18 (2026) 100557

Contents lists available at ScienceDirect

Carbon Capture Science & Technology

journal homepage: www.elsevier.com/locate/ccst

Full Length Article

Carbonation behavior of reactivated recycled concrete fines containing residual sand: Effects of Ca/Si ratio adjustment and activation temperature

Yutong Ju [a], Ye Li [a], Xiangping Xian [b], Tiejun Liu [a,*]

[a] School of Civil and Environmental Engineering, Harbin Institute of Technology, Shenzhen, 518055, China
[b] Department of Architecture and Civil Engineering, City University of Hong Kong, 83 Tat Chee Avenue, Hong Kong, Kowloon Tong, 999077, China

ARTICLE INFO

Keywords:
Recycled concrete fines
Residual sand particles
Thermal activation
Reactivated binders
Carbonation curing

ABSTRACT

The valorization of recycled concrete fines (RCF) into reactive binders offers a sustainable solution for mitigating construction waste and carbon emissions. However, embedded sand particles hinder phase development during thermal activation. This study explores thermally activated sand-containing RCF by adjusting calcium-to-silicon ratio via limestone addition to produce reactivated cementitious materials (RCM). Carbonation-cured RCMs were analyzed for phase evolution, microstructure, and strength. Results showed that higher activation temperature with Ca addition enhanced sand reactivity and mineral formation, transitioning from α'_H-C_2S and β-C_2S below 1000 °C to low-reactivity CS or C_3S_2 at 1200 °C. Carbonation curing of RCM activated at 1000 °C with 20 wt.% limestone addition yielded the highest mechanical performance by optimizing phase reactivity, carbonation efficiency, and pore refinement, while lower strengths in other groups stemmed from insufficient $CaCO_3$ and silica gel. Life cycle assessment showed a 61 % CO_2 reduction compared to Portland cement, which validates thermochemical tuning for closed-loop RCF recycling.

1. Introduction

The rapid acceleration of global urbanization and urban renewal has resulted in a dramatic surge in waste concrete generation, exceeding 3 billion tons annually (Fang et al., 2024; Pristerà et al., 2024). Conventional disposal methods–such as dumping and landfilling–not only consume valuable land resources but also present serious environmental hazards (Duan and Li, 2016; Ram et al., 2020). Reusing waste concrete into recycled aggregates (particles larger than 4.75 mm) and recycled sands (particles between 0.125 mm and 4.75 mm) offers a sustainable alternative to address both environmental challenges and resource scarcity (Infante Gomes et al., 2021; Liu et al., 2022). However, a significant amount of recycled concrete fines (RCF) is inevitably generated during the production of recycled aggregates, accounting for over 20 wt. % of waste concrete (Tang et al., 2020). The utilization of this RCF fraction is crucial for achieving full-component recycling of waste concrete.

Various techniques have been explored to valorize RCF as alternative binders and novel cementitious systems, including carbonation, chemical leaching, alkali activation, and thermal activation (Mao et al., 2024a, 2024b; Shen et al., 2022a). Among these, thermal activation is regarded as a highly industrialized technical route due to its ability to utilize existing or decommissioned cement kilns, minimize capital investment while offering large-scale processing capacity. Because RCF is rich in calcium silicate hydrates (C–S–H) and calcium hydroxide, heating to between 400 °C and 1200 °C (Bogas et al., 2020; Serpell and Lopez, 2013; Shui et al., 2009; Xu et al., 2022) leads to C–S–H and calcium hydroxide in RCF dehydrate and form reactive silicate phases, effectively regenerating a low-calcium cementitious material (Crook and Murray, 1970; Miller et al., 2016; Real et al., 2020; Wang et al., 2018). Despite this promise, a critical limitation in current thermal activation research is its predominant focus on pure hardened cement pastes as precursor material (Carriço et al., 2020; Kalinowska-Wichrowska et al., 2019; Miller et al., 2016; Real et al., 2020; Wang et al., 2018; Xi et al., 2024; Xu et al., 2023; Zanovello et al., 2024; Zhu et al., 2018), neglecting sand–a major constituent of waste concrete.

Sand primarily composed of low-reactivity crystalline α-SiO_2, altering the chemical composition (especially calcium-to-silicon ratio) of pure hydration products during thermal activation (Abo-Almaged et al., 2024; Autef et al., 2012; Bogas et al., 2020; Ji et al., 2024). A temperature exceeding 1150 °C caused sand melting and fusing with cement (Ge et al., 2025), revealing sand's potential as a reactive silica

* Corresponding author.
E-mail addresses: 24b954007@stu.hit.edu.cn (Y. Ju), liye0006@e.ntu.edu.sg (Y. Li), xiangping.xian@cityu.edu.hk (X. Xian), liutiejun@hit.edu.cn (T. Liu).

https://doi.org/10.1016/j.ccst.2025.100557
Received 14 October 2025; Received in revised form 3 December 2025; Accepted 14 December 2025
Available online 15 December 2025

source. Viggh et al. (Viggh et al., 2020) discovered that the source of quartz would affect the formation of belite. Luo et al. (Luo et al., 2025) prepared dicalcium silicate using desert sand at 1030 °C. Abdelghani et al. (Brahimi et al., 2020) prepared a new green cementitious material based on Algerian sand dune. These findings support the concept that sand could be combined with hydration products and calcium source to produce novel low-calcium cementitious binders. Limestone ($CaCO_3$) was selected as the calcium source due to its central role in conventional cement production, its low cost and chemical stability, and its compatibility with large-scale kiln processing. During thermal activation, $CaCO_3$ decomposes in situ to form highly reactive CaO, which effectively reacts with SiO_2 from both dehydrated C–S–H and sand particles to promote the controlled formation of calcium silicate phases. This provides a direct and industrially relevant route for Ca/Si ratio regulation in sand-containing RCF systems.

Another common issue with thermally reactivated cementitious materials (RCM) is their low compressive strength, often around only 10 MPa after one week under conventional conditions, due to the low hydraulic reactivity of the formed silicate minerals (Bogas et al., 2019, 2020; Carriço et al., 2020; Shui et al., 2008; Wang et al., 2018; Xu et al., 2023). Carbonation curing dramatically improves mechanical performance, enabling strengths exceeding 60 MPa for γ-dicalcium silicate (γ-C_2S) (Zhao et al., 2021), 66 MPa for rankinite (C_3S_2) and 20 MPa for wollastonite (CS) (Mu et al., 2019). These improvements not only broaden application of RCM (Lu et al., 2021; Wang et al., 2022), but also enables CO_2 sequestration and reduces carbon emissions.

This study tests the hypothesis that strategic limestone addition can effectively regulate the Ca/Si ratio in sand-containing recycled concrete fines (RCF), thereby promoting the formation of reactive calcium silicate phases through solid-state reactions during thermal activation. It further hypothesizes that the resulting phase assemblage directly governs the carbonation mechanism, as well as the type and crystallinity of $CaCO_3$ polymorphs and the degree of microstructural densification. Finally, it is hypothesized that these coupled mineralogical and microstructural changes lead to enhanced mechanical performance and a reduced carbon footprint of the reactivated cementitious materials. To validate these hypotheses, the mineral composition of the reactivated cementitious materials (RCM), the phase assemblage and microstructure of the carbonation products, and the mechanical performance were systematically characterized using X-ray diffraction (XRD), thermogravimetric analysis (TGA), mercury intrusion porosimetry (MIP), scanning electron microscopy (SEM), and compressive strength tests. The carbon footprint was further quantified using life cycle assessment (LCA). This study aims to establish the feasibility of thermally activating sand-containing RCF, elucidate the role of calcium supplementation in enhancing reactivity, and advance comprehensive waste concrete recycling.

2. Materials and specimen preparation

2.1. Raw materials

In this study, recycled concrete fines (RCF) refer to fine recycled concrete-derived materials containing both hydrated cement pastes and residual sand phases obtained after crushing and grinding of waste mortar. P.O. 42.5 R cement (OPC, Anhui Conch Cement Co., Ltd) and ISO standard sand (0.08–2.0 mm; <0.2 % moisture) were served as primary raw materials to prepare simulated RCF. Analytically pure reagents such as calcium carbonate (≥ 99.0 %), isopropanol (≥ 99.7 %), ethanol (≥ 99.7 %), and zinc oxide (≥ 99.0 %) were sourced from Sinopharm Chemical Reagent Co., Ltd. Tap water in the laboratory was used for sample preparation. X-ray diffraction (XRD) pattern and X-ray fluorescence spectrometry (XRF) results of OPC identified phases as C_3S, β-C_2S, C_4AF, C_3A, $CaCO_3$, and $CaSO_4$, as detailed in Fig. 1 and Table 1.

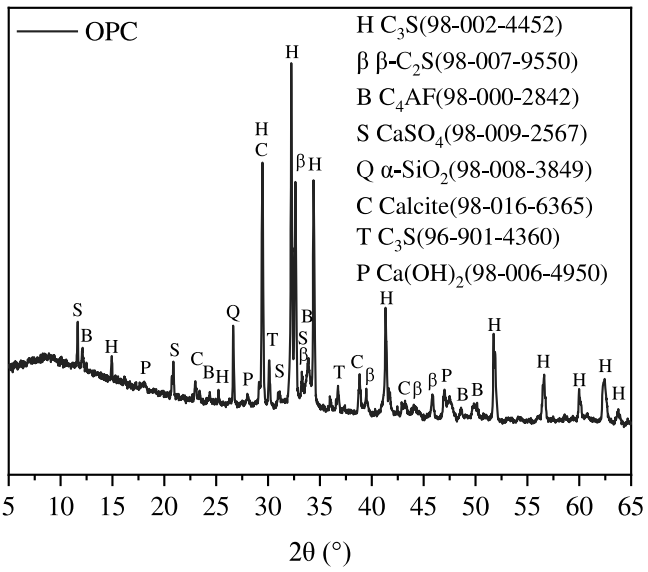

Fig. 1. Phase assemblage of OPC.

2.2. Preparation of reactivated cementitious materials

Simulated RCF, referred to as waste mortar, was prepared with a binder-to-sand ratio of 1 to 2 and a water-to-binder ratio of 0.4. The use of a synthesized OPC–standard sand system was a methodological choice aimed at establishing a well-defined, reproducible, and compositionally controlled model system. This approach enables investigation of the intrinsic high-temperature reactions between cement hydration products and silica, as well as the controlled regulation of the Ca/Si ratio, without the confounding effects of the highly variable cement types and supplementary cementitious materials typically present in real RCF. Although the present study does not attempt to represent the full compositional diversity of all real RCF, the proposed methodology is broadly representative and transferable. Regardless of the original concrete composition, RCF with different initial Ca/Si ratios can be adjusted using the same approach by modifying calcium source dosage, while the underlying reaction mechanisms, phase evolution pathways, and carbonation principles remain applicable after appropriate precursor characterization and Ca-source calibration.

The mortar was water-cured for three months and aged indoors at 20 ± 2 °C and 60 ± 5 % RH for five months. This extended regime was designed to achieve a high degree of hydration (>80 %) and a mature microstructure, representative of a well-hydrated cement paste (Termkhajornkit et al., 2015; Wong and Buenfeld, 2009). The cured mortar was crushed into 1 cm fragment, ground by a planetary mill (650 rpm, 15 min), and sieved (<75 μm) to obtain RCF.

XRF analysis revealed elevated silicon content in RCF due to inclusion of sand (Table 1). Calcium carbonate was added to adjust the Ca/Si ratio to target values of CS (1), C_3S_2 (1.5), C_2S (2), and C_3S (3). For example, achieving Ca/Si=2 required 39.19 wt. % calcium carbonate as shown in Eq. (1), with calculated values rounded to 10 % increments (Table 2).

$$Ca\Big/Si=\frac{\left(\frac{m_{CaO}\cdot(100-x)}{Mr_{CaO}}+\frac{x}{Mr_{CaCO_3}}\right)}{\frac{m_{SiO_2}\cdot(100-x)}{Mr_{SiO_2}}}=2 \quad (1)$$

where m_{CaO}, m_{SiO_2} represent the contents of calcium oxide (CaO) and silicon dioxide (SiO_2) in RCF. Mr_{CaO}, Mr_{CaCO_3} and Mr_{SiO_2} were the relative molecular masses of CaO, $CaCO_3$, and SiO_2, which are 56, 100, and 60, respectively.

Thermal activation involved several steps, including mixing,

Table 1
Chemical composition of OPC and RCF (wt. %).

Ingredient	CaO	SiO_2	Al_2O_3	Fe_2O_3	MgO	K_2O	SO_3	SrO
OPC	61.64	21.54	5.70	3.30	2.93	1.07	3.24	0.07
RCF	43.28	42.96	5.21	3.06	1.91	0.50	2.13	0.03

Table 2
The mass fraction of the extra added calcium carbonate.

Target Ca/Si ratio	Theoretical additions (wt. %)	Experimental additions (wt. %)	Practical Ca/Si ratio
1.08 (initial value)	/	0	1.08
1.5	22.63	20	1.43
2	39.19	40	2.01
3	57.33	60	3.17

compacting, calcining, rapid cooling, milling, and sieving, as illustrated in Fig. 2. The precursors were mixed in a three-dimensional blender for 24 h. A 30 g mixture, with 10 % added tap water by weight, was compacted into cylinders (Φ40 mm × 10 mm) at a pressure of 20 MPa. These cylinders were calcined in a muffle furnace at a rate of 10 °C/min to target temperatures of 800 °C, 1000 °C, and 1200 °C, maintained for 3 h. The thermal activation temperatures (800 °C, 1000 °C, and 1200 °C) were chosen to cover a critical range: from the decomposition temperature of cement hydrates at the lower end, up to and beyond the point where partial sand fusion and enhanced solid-state reactions with cement phases become significant, as reported in literatures (Ge et al., 2025; Li et al., 2023; Ren et al., 2025). After calcination, samples were rapidly cooled by the wind, re-milled at 300 rpm, and sieved to obtain the final RCM product (<75 μm). After calcination, the crucible containing the hot sample was immediately removed from the furnace and placed in a designated cooling area at a controlled ambient temperature of 25 ± 3 °C. A laboratory air blower was positioned at a fixed distance of 20 cm from the sample to provide directed forced convection. Under these conditions, the sample was cooled to room temperature within approximately 20 min. Samples were designated M-T-CC (material, temperature, calcium carbonate content), with untreated RCF stored at 20 °C as control (M-20-0).

2.3. Carbonation curing of specimens

RCM specimens were cast into 25 mm cubic molds with a water-to-solid ratio of 0.4, following procedures in references (Mucsi et al., 2021; Wang et al., 2020; Zhao et al., 2021). After setting for six hours, specimens were transferred to a carbonation chamber holding for 7 days, maintained at 70 % ± 5 % relative humidity, 20 % ± 2 % CO_2 concentration, and 40 ± 2 °C. The carbonation curing regime was selected based on our previous foundational research (Li et al., 2023; Liao et al., 2024). Specimens were designated as C-T-CC, categorized by carbonation conditions (C), thermal activation temperature (T), and calcium carbonate addition (CC).

3. Characterization methods

Thermal-activated and carbonated RCM samples were preserved in isopropanol to halt hydration and carbonation processes. These samples were subsequently ground manually and sieved through a 75 μm mesh for analysis. All powder samples for tests were obtained from a single homogenized batch for each group, ensuring different tests were performed on representative material.

TGA was conducted on a Netzsch STA 449 F5/F3 Jupiter instrument. For thermal activation of RCM precursor, blended samples were heated from 30 °C to 1500 °C in a nitrogen atmosphere at a rate of 10 °C/min. For phase analysis of carbonated and hydration products, a temperature range of 30 °C to 900 °C was adopted. The mass of TGA was 15 ± 2 mg. The mass change measured by thermogravimetric analysis was reported on a percentage basis. XRD analysis employed a Bruker D8 Advance X-ray powder diffractometer (Cu Kα radiation, 40 kV, 40 mA) scanning from 5° to 65°, with a total scan duration of 20 min. 10 wt. % zinc oxides (ZnO) as the internal standard for standard for quantitative analysis. The XRD patterns were analyzed using software HighScore Plus 3.0.

Pore size distribution was evaluated using a Micromeritics Autopore IV 9500 mercury porosimeter. Small cube samples (~5 mm) were exclusively cored from the central region of the carbonated specimens, and all selected samples were visually inspected to be free of cracks and major defects. The pore sizes between 6 nm and 360 μm were measured.

SEM imaging was performed using a Phenom ProX G6 SEM equipped with backscattering mode and energy-dispersive X-ray spectroscopy (EDS). For thermal-activated RCM samples, the specimens were impregnated with resin and allowed to set for 24 h. The surfaces were prepared by sequential grinding and polishing using sandpaper ranging from 600 to 2400 grit, followed by polishing with 3 μm to 1 μm polishing paste to achieve smooth surfaces. For carbonated specimens, the morphology was observed directly by placing small broken pieces (side lengths <5 mm) into the SEM chamber. These samples were scanned in secondary electron mode at an accelerating voltage of 15 kV to capture detailed surface structures.

Compressive strength of carbonated RCM specimens was measured using a SANS universal testing machine from MTS LTD at a constant

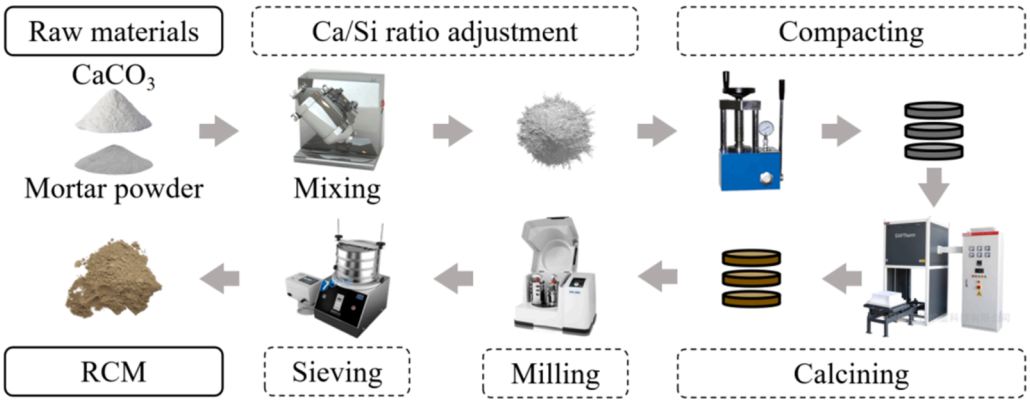

Fig. 2. Process of RCM preparation.

displacement rate of 0.5 mm/min (Mu et al., 2019; Wang et al., 2020). All tests were performed in triplicate, and the results are reported as mean values with standard deviations to ensure statistical reliability.

4. Results and discussion

4.1. Phase assemblage of the RCM

4.1.1. Effect of activation temperatures

TGA with derivative thermogravimetric curve (DTG curve) and differential scanning calorimetric curve (DSC curve) was performed on RCF without the addition of calcium carbonate up to 1500 °C, revealing phase transformations during thermal treatment. The DTG curve in Fig. 3 showed a peak around 100 °C, corresponding to free water evaporation (Alarcon-Ruiz et al., 2005). Peaks between 180 °C and 450 °C represented C–S–H dehydration (Alonso and Fernandez, 2004; Xu et al., 2022). The peak near 450 °C of DTG and DSC curves indicated that calcium hydroxide absorbed heat and dehydroxylated (Alarcon-Ruiz et al., 2005), leading to 1.7 wt. % loss of mass. The endothermic peak at ~647 °C corresponds to the thermal decomposition of calcium carbonate formed by natural carbonation of RCF (Saeki et al., 2024). The mass loss between 500 and 700 °C is attributed to the decomposition of C–S–H into C_2S polymorphs (α'_H-C_2S, β-C_2S, and γ-C_2S), with a mass loss of approximately 4.9 wt. % (Handoo et al., 2002; Okada et al., 2005; Peng and Huang, 2008). This interpretation is consistent with the QXRD results in Fig. 4, which confirm the disappearance of $Ca(OH)_2$ and $CaCO_3$ and the emergence of C_2S after activation at 800 °C. The thermal feature near ~850–900 °C is assigned to the formation of gehlenite via solid-state reactions among CaO, SiO_2, and Al_2O_3 (Xu et al., 2021). The peak at ~1072 °C signals the formation of wollastonite, which is independently confirmed by QXRD, with wollastonite contents of 4.3 % at 1000 °C and 37.1 % at 1200 °C. Further, calcium carbonate addition facilitated C_3S_2 formation, which will be detailed in Section 4.1.2. As the peak appeared at 1331 °C, C_3S began to generate when the temperature was over 1250 °C (Zhutovsky and Shishkin, 2021).

Quantitative X-ray diffraction (QXRD) was conducted on RCM at varying activation temperatures, as shown in Fig. 4. This analysis details the transformation of calcium silicate minerals in RCF without modifying the Ca/Si ratio as activation temperatures increase. At 800 °C and 1000 °C, RCM primarily contained α'_H-C_2S and β-C_2S with a total content of 28.2 %. At 1000 °C, more C_2S was generated with a content of 35.2 %. However, α'_H-C_2S decreased significantly, with β-C_2S becoming dominant. This phenomenon appears in other references as well (Serpell and Zunino, 2017; Zhutovsky and Shishkin, 2021). The rapid cooling after activation at 1000 °C promotes the retention of β-C_2S and the complete transformation of α'_H-C_2S (Serpell and Lopez, 2015). At 1200 °C, C_2S reduced while wollastonite and pseudowollastonite peaked at 37.1 %.

Untreated RCF contains about 33 % amorphous substances,

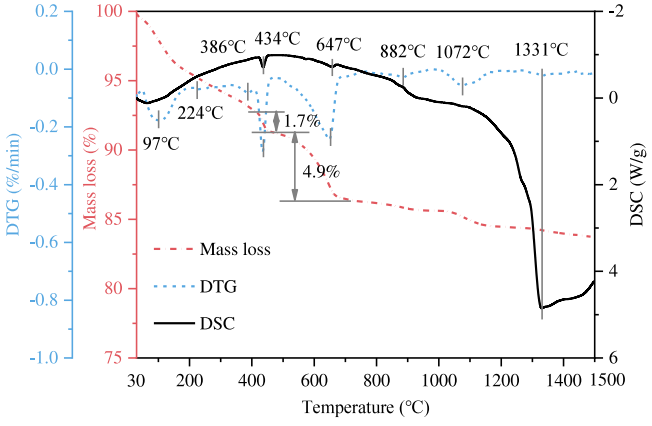

Fig. 3. TGA results of RCF.

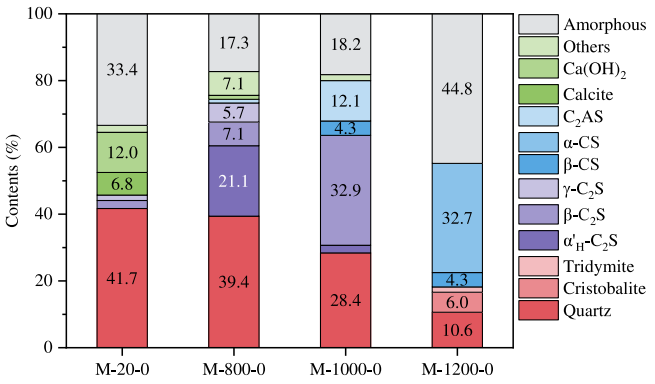

Fig. 4. QXRD results of the RCM with different activation temperatures.

primarily C–S–H gels from the hydration of C_2S and C_3S (Beaudoin and Odler, 2019), along with possible alumina gels from C_3A and C_4AF hydration (Bullard et al., 2011; Cai et al., 2021). Activated at 800 °C, C–S–H degrades, forming calcium silicates (C_3S and C_2S) (Amiri et al., 2022; Zheng et al., 2021), while poorly crystallized C_2S and unreacted C–S–H gels remain (Sun et al., 2024). As temperature rises, crystalline C_2S increases and amorphous content decreases, aligning with findings by Li et al (Li et al., 2021). At 1200 °C, amorphous substances rise, likely due to poor crystalline CS minerals from C_2S-sand reactions and C–S–H gel transformation (Amiri et al., 2022; Li et al., 2023; Trník et al., 2016; Zheng et al., 2021). Additionally, hydration products containing aluminum like ettringite decompose, yielding $C_{12}A_7$ (Lee et al., 2017b), while C–(A)–S–H gels convert to gehlenite (Lee et al., 2017a).

Increased activation temperatures accelerated sand reaction and calcium silicate formation. The main phases formed have decreased hydration activity but can be effectively carbonated. This will be reflected in the following sections.

4.1.2. Effect of calcium-silicon ratio adjustment

Fig. 5 displayed XRD patterns for RCMs activated at 800 °C. The M-800-60 means that addition of 60 wt. % calcium carbonate prior to activation. All samples showed diffraction peaks for α'_H-C_2S, β-C_2S, γ-C_2S, CS, C_4AF, $C_{12}A_7$ and quartz. "Others" in Fig. 5(b) represents a marginal amount of C_3S, gypsum, and gehlenite. A pronounced increase in calcite peak intensity was observed with higher calcium carbonate addition, concurrently with a reduction in SiO_2 peak intensity near 27°. The reduced sand content implies participation in solid-phase reactions during thermal activation. However, incomplete decomposition of the added calcite occurred, resulting in higher residual content: 19.2 % in M-800-20, 34.2 % in M-800-40, and 43.0 % in M-800-60. Only 0.8 %, 5.8 %, and 17.0 % of added calcium carbonate decomposed and the resultants reacted with quartz at 800 °C. This incomplete reaction directly suppressed C_2S formation, evidenced by its decrease from 33.9 % in M-800-0 to 21.8 % in M-800-60. The accumulation of residual calcite and reduced C_2S yields indicates limited effectiveness in adjusting the Ca/Si ratio.

Fig. 6 presented XRD patterns and phase proportion for RCMs activated at 1000 °C. A significant substance transformation occurred compared to M-20-0. Specifically, phases such as $Ca(OH)_2$, $CaCO_3$, and $CaSO_4$ were replaced by more stable phases like C_2S, CS, and gehlenite (C_2AS). The interaction of SiO_2 from RCF with decomposed CaO predominantly led to the formation of β-C_2S. Additionally, dehydration of C–S–H gel also contributed to development of β-C_2S, which emerged as the dominant phase, constituting 32.9 %, 43.2 %, 34.1 %, and 39 % in M-1000-0, M-1000-20, M-1000-40, and M-1000-60, respectively. The high reliability of the quantification was validated by the good fit (R-weighted pattern, Rwp < 15 %) achieved for all samples. Detailed data was recorded in Table S1 of the supplementary materials. Notably, α'_H-C_2S was minimal (2.3 % only in M-1000-0) and γ-C_2S was absent,

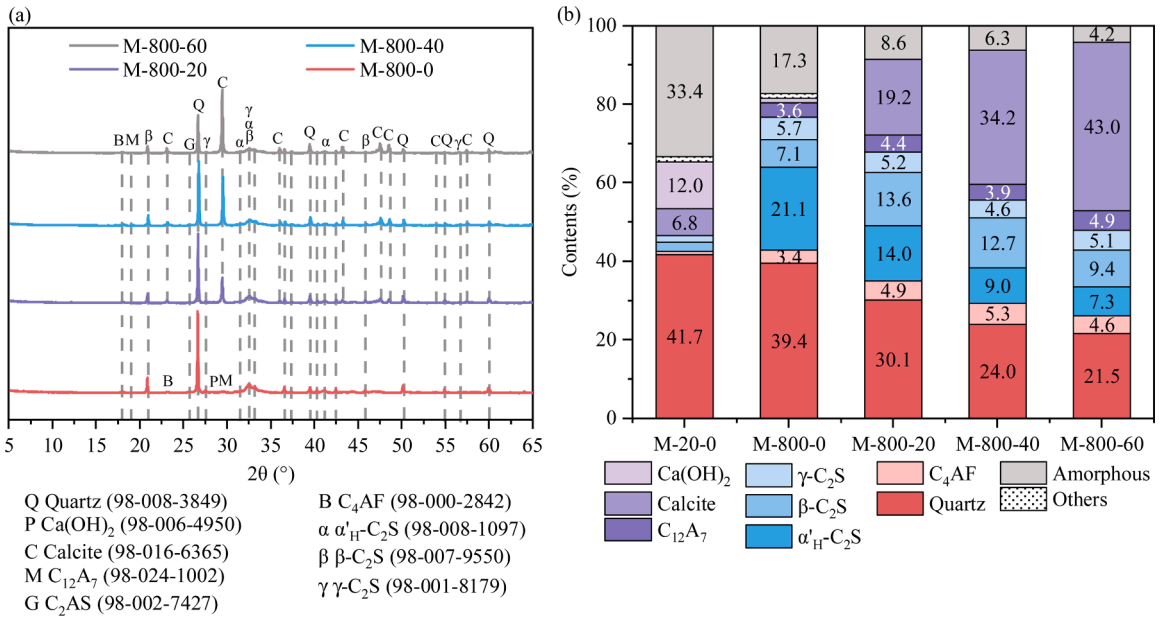

Fig. 5. XRD results of the RCM activated at 800 °C (a) XRD patterns and (b) QXRD results.

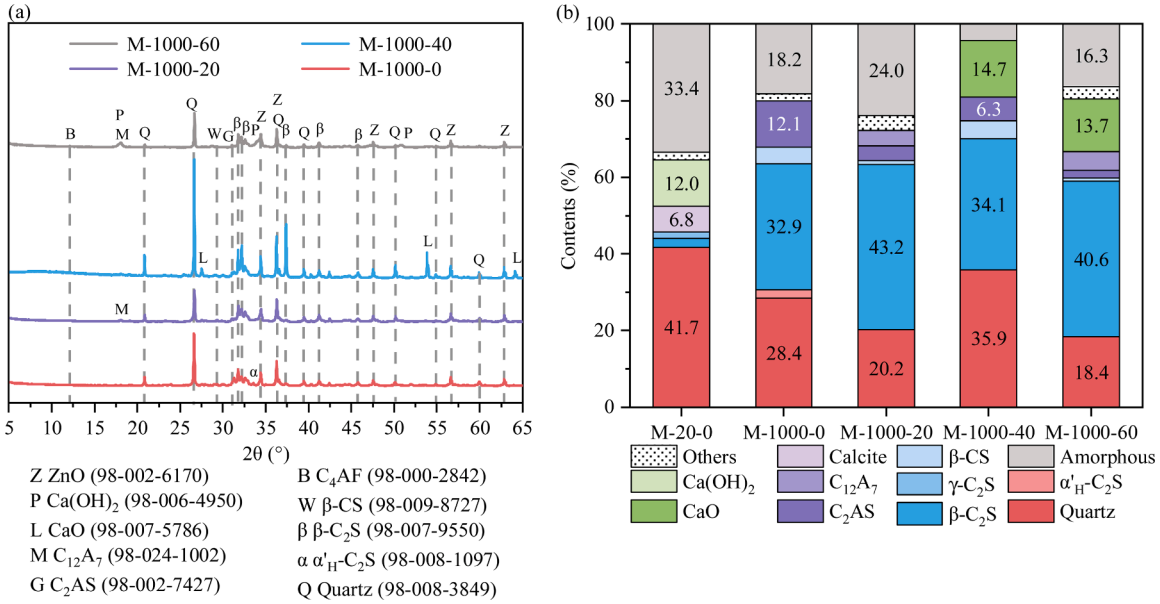

Fig. 6. XRD results of the RCM activated at 1000 °C: (a) XRD patterns and (b) QXRD results.

confirming the stability of β-C_2S. This observation was consistent with the findings of Zhong et al. (Ávalos-Rendón et al., 2018), attributing β-C_2S stability to rapid cooling process inhibiting its transformation to γ-C_2S. Furthermore, calcium oxide reacted with aluminum and silicon compounds to form C_2AS. Content of C_2AS diminished sharply from 12.1 % to 2.0 % with increasing calcium carbonate, suggesting that higher calcium levels favor C_2S while suppressing the generation of C_2AS (Xu et al., 2021).

Compared with the sand content of M-20-0 (45.5 %), the M-1000-0, M-1000-20, M-1000-40, and M-1000-60 contained of 28.4 %, 20.2 %, 35.9 % and 17.7 % residual sand respectively, indicating substantial participation of sand in solid-state reactions during thermal activation at 1000 °C. The decrease in residual sand signifies its direct consumption and transformation into new solid phases, rather than being physically removed. However, residual calcium oxide persisted in M-1000-40 (14.7 %) and M-1000-60 (13.7 %) with extra $CaCO_3$, indicating incomplete consumption of the added calcium carbonate. It implies diminishing returns at higher calcium carbonate dosages at 1000 °C.

Most importantly, the phase assemblage directly governed the mechanical performance. The high β-C_2S content, particularly in M-1000-20, was the primary factor responsible for the superior compressive strength observed after carbonation curing (Fig. 17). In contrast, the persistence of substantial unreacted CaO in M-1000-60 was associated with inferior strength development.

Fig. 7 presents the XRD analysis for RCMs activated at 1200 °C. Diffraction peaks confirmed the formation of calcium silicate minerals such as wollastonite (β-CS) and pseudowollastonite (α-CS), aligning with TGA curves (Fig. 3). Additionally, C_3S_2 appeared in the M-1200-40 and M-1200-60. Transformation of quartz to high-temperature polymorphs tridymite and cristobalite was detected (Pagliari et al., 2013).

The adjustment of the Ca/Si ratio at 1200 °C had a significant impact on the phase composition of the RCM. Increases in calcium carbonate

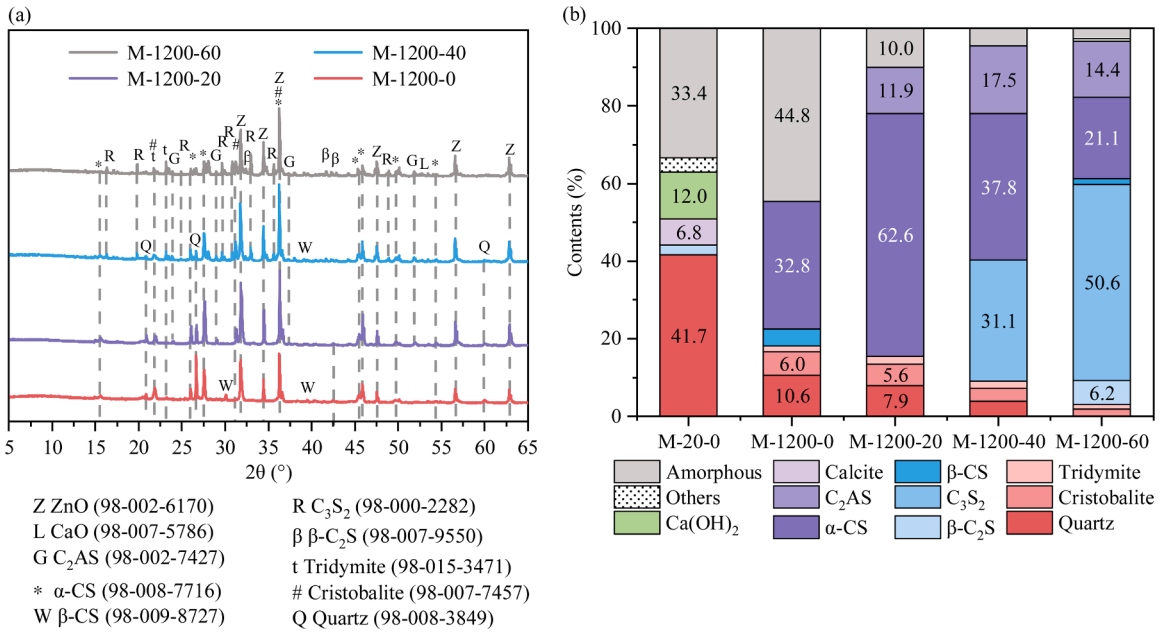

Fig. 7. XRD results of the RCM activated at 1200 °C: (a) XRD patterns and (b) QXRD results.

boosted wollastonite and pseudowollastonite formation. At 40 wt. % addition, C_3S_2 emerged, increasing to 50.6 % at 60 wt. % addition. β-C_2S was detected in M-1200-60 (6.2 %), while α'_H-C_2S and γ-C_2S were absent. The cumulative content of calcium silicate minerals (C_2S, C_3S_2, CS) rose from 37 % (M-1200-0) to 79 % (M-1200-60). Residual sand content decreased consistently with higher calcium carbonate, mirrored by reductions in the total SiO_2 content (18.1 % to 3.0 %). The increase in calcium silicate minerals and the decrease in sand jointly indicate that increased calcium carbonate dosage promotes participation of sand in RCM synthesis reaction.

4.2. Microscopic morphology of the RCM

4.2.1. Effect of activation temperatures

The microscopic morphology of thermally activated RCM was examined using SEM-EDS. Fig. 8 presented the EDS mapping results for RCM activated at three different temperatures. The mapping revealed that calcium (colored red) accumulated around sand particles, forming a distinct ring of newly generated calcium-containing phase. This calcium-rich ring became more pronounced as the activation temperature increased, visually confirming that higher temperatures enhance the incorporation of calcium into the sand particles. This change was consistent with the XRD results discussed in Section 4.1. At 1200 °C, many sand particles transformed into a new phase containing both calcium and silicon, indicative of the formation of CS (as shown in

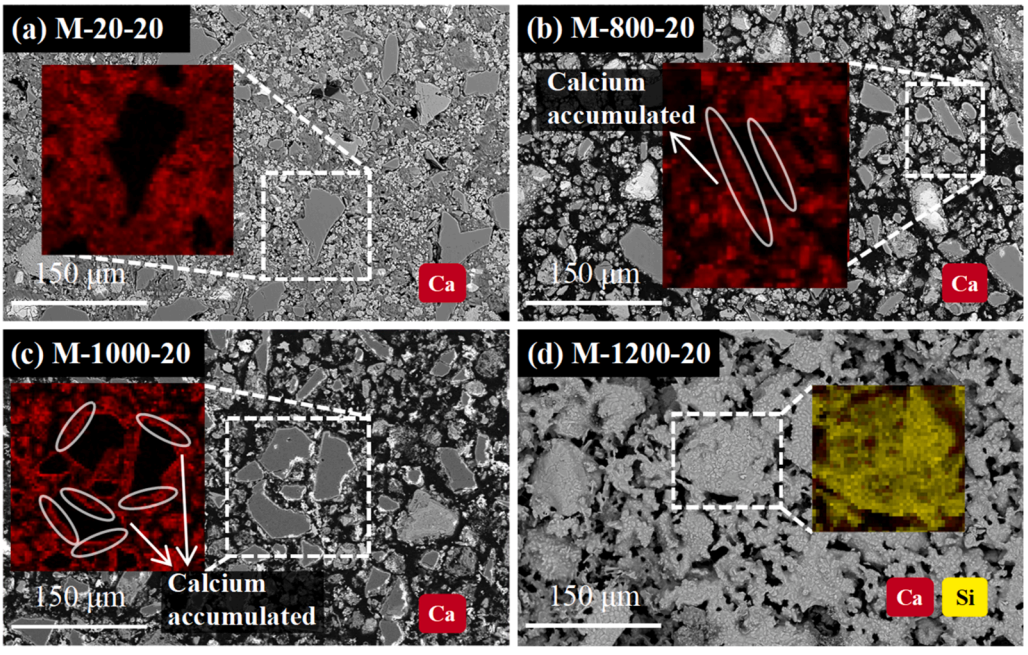

Fig. 8. EDS mapping results of (a) the RCF and the RCM activated at (b) 800 °C, (c) 1000 °C, and (d) 1200 °C.

Fig. 12).

Fig. 9 showed the EDS line scanning results for the M-1200-0 group, where the distribution and concentration of elements (O, Si, and Ca) were measured along a 19.08 μm line with 128 measurement points. In the first half of the scan (0–9.54 μm), the concentrations of silicon and oxygen remained stable, with silicon fluctuating between 22 % and 25 % and oxygen maintaining a concentration of 75 %. Notably, calcium was absent in this segment, consistent with the elemental composition of sand. However, from 9.54 μm to the endpoint (19.08 μm), a sharp increase in calcium concentration (reaching 27 %) was observed, accompanied by a correspondingly decreased in oxygen concentration to 27 %. This shift suggests the formation of CS and highlights the transformation of quartz. The relatively stable silicon content throughout the scan further demonstrates the movement of calcium and oxygen atoms, while silicon remains largely unchanged.

4.2.2. *Effect of calcium-silicon ratio adjustment*

The influence of Ca/Si ratio adjustment on RCM microstructure was analyzed using SEM, with EDS results presented in Figs. 10–12. As presented in Fig. 10(a), the sand particles initially exhibited sharp edges and uniform grayscale, surrounded by unhydrated cement particles and hydration products. However, after activation at 800 °C as demonstrated in Fig. 10(b), the interface between the sand and surrounding mortar matrix appeared brighter, indicating localized interfacial reactions within several microns. In contrast, the internal areas of the sand particles were dark. Despite varying calcium carbonate additions (20 %–60 %), the overall morphology of the sand remained relatively unchanged, as shown in Fig. 10(c) to (e).

At 1000 °C (Fig. 11), the central regions of the sand present Ca/Si ratios of 0.01–0.02. Compared with M-20-0 (as shown in Fig. 10), thermal activation at 1000 °C led to the formation of a ring of short rod-like crystals around the sand particles. EDS point analysis revealed that these crystals exhibited the Ca/Si ratio of 1.68–2.38, characteristic of C_2S, in agreement with the XRD results in Section 4.1. Increasing the calcium carbonate content resulted in denser and more widely distributed rod-like crystals, particularly evident in Fig. 11(d).

Fig. 12 illustrated the microstructural evolution of RCM activated at 1200 °C, where sand particles underwent significant transformation into densely packed, irregular ellipsoidal crystals extending from the surface to the core. The blurry boundaries around these crystals suggested extensive integration with surrounding products, identified by XRD analysis in Section 4.1 as predominantly calcium silicate minerals, including CS and C_3S_2 (Fig. 7). EDS point analysis showed Ca/Si ratios close to 1.0 in M-1200-0 and M-1200-20, consistent with CS. In M-1200-40, Ca/Si ratios of 1.0 and 1.5 corresponded to CS and C_3S_2, respectively. With an increase in calcium carbonate to M-1200-60, varied Ca/Si ratios of 1.0, 1.2, and 1.8 were identified, which corresponded to CS, C_3S_2, and C_2S, aligning with the XRD findings.

The data suggests that higher activation temperatures substantially enhance the reaction of sand particles, promoting the formation of larger calcium silicate crystals, particularly at 1200 °C. While calcium carbonate addition has limited effects at 800 °C, it significantly contributes to the formation at 1200 °C. Adjusting the Ca/Si ratio through calcium carbonate addition and increased temperature significantly alter the microstructure and phase composition of RCM. The impact of these changes on the carbonation process and mechanical properties will be further discussed in subsequent sections.

This study employed a mixture of OPC and standard sand as a model RCF system to isolate and elucidate fundamental reaction mechanisms under controlled conditions. However, real-world RCF exhibits greater compositional and microstructural heterogeneity, which may significantly influence thermal activation behavior and the performance of the resulting RCM. The chemical composition of cement paste in waste concrete can vary due to differences in cement type, the presence of supplementary cementitious materials (SCMs) such as fly ash and slag, and residual chemical admixtures. These constituents may modify both the decomposition temperatures and the phase evolution pathways during thermal activation. For example, SCM-derived alumina and silica may promote the formation of alumino-silicate phases such as gehlenite at the expense of calcium silicate phases, thereby altering the reactivity and carbonation potential of RCM. In addition, the presence of carbonate aggregates (e.g., limestone) or clay-bearing fines in real RCF may participate in high-temperature solid-state reactions, potentially leading to the formation of clinker-like phases or amorphous glassy products not observed in the present model system. These factors indicate that the optimal activation parameters identified herein may require case-specific adjustment for different real RCF sources.

4.3. *Phase assemblage of the carbonated specimens*

The effects of activation temperature and Ca/Si ratio adjustments on the carbonation behavior of hardened RCM were analyzed through XRD results, as depicted in Fig. 13. When RCM prepared at 800 °C shown in Fig. 13(a), carbonated specimens exhibited diffraction patterns comprising calcite, vaterite, unreacted sand, and small amounts of C_2S polymorphs. The calcite originated from both carbonation reactions of RCM and the residual calcium carbonate in precursors. Notably, C-800-0 sample without externally added calcium carbonate, contained 25.8 % vaterite alongside 11.1 % calcite. In contrast, samples with externally added calcium carbonate (C-800-20/40/60 samples) showed no detectable vaterite. This difference arises because vaterite, a metastable polymorph, initially precipitates during carbonation but rapidly converts to calcite (Chang et al., 2016) in the presence of residual calcium carbonate (calcite), which act as nucleation sites (Zhao et al., 2024).

When RCM prepared at 1000 °C, all externally added calcium carbonate decomposed during activation. The calcite content in the carbonated samples increased, starting from 19.3 % (C-1000-0) to 41.3 % (C-1000-60) as attained from Fig. 13(d). Conversely, vaterite content

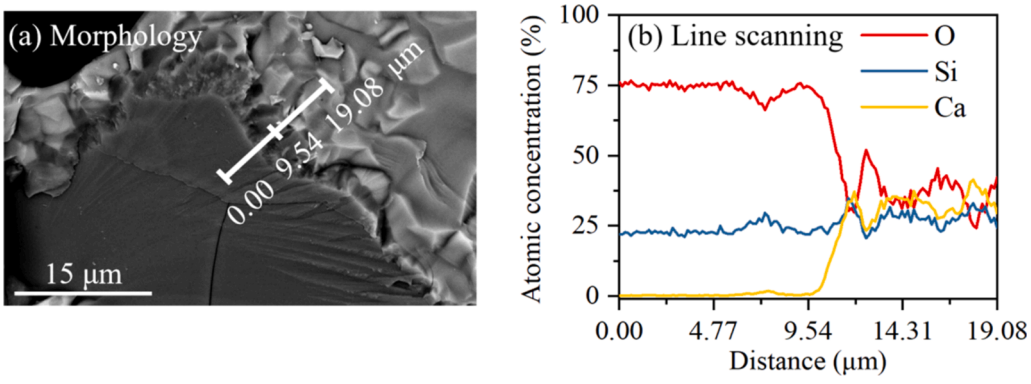

Fig. 9. EDS results of M-1200-0 with (a) morphology and (b) line scanning results.

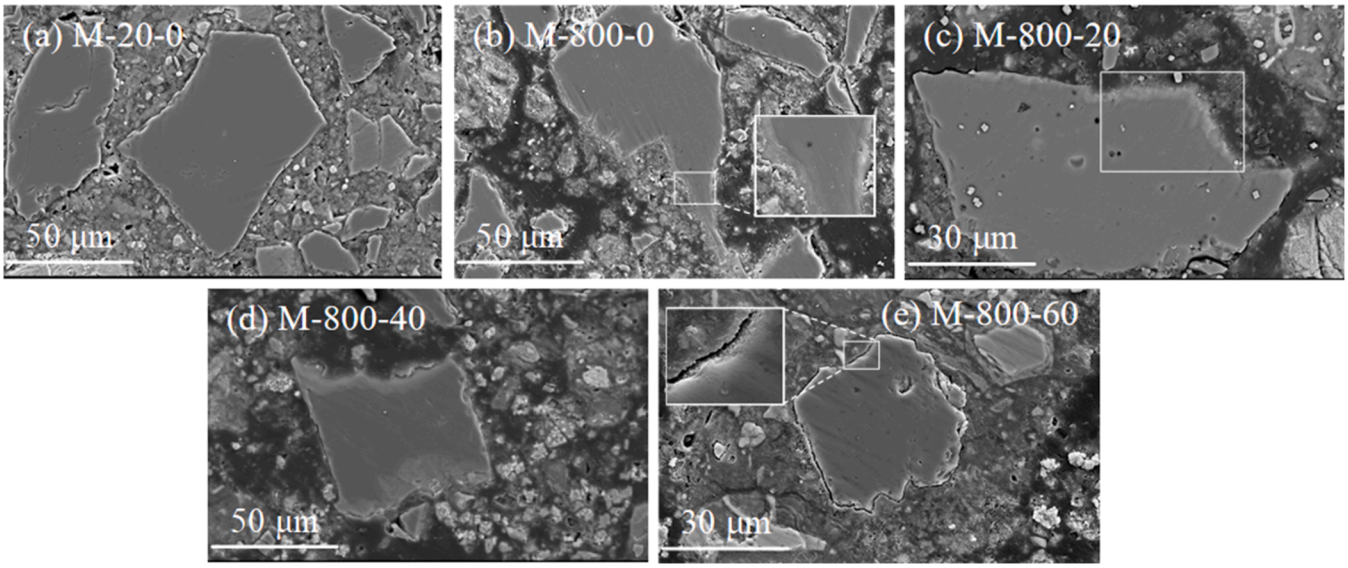

Fig. 10. Morphology of the RCM activated at 800 °C. (a) M-20-0, (b) M-800-0, (c) M-800-20, (d) M-800-40, and (e) M-800-60.

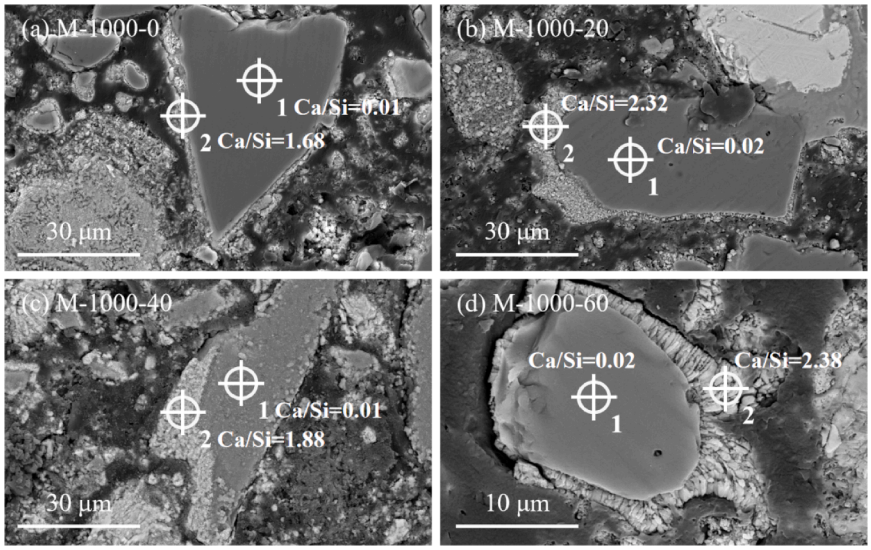

Fig. 11. Morphology of the RCM activated at 1000 °C. (a) M-1000-0, (b) M-1000-20, (c) M-1000-40, and (d) M-1000-60.

peaked at 10.3 % (C-1000-20) but decreased to 2.6 % in C-1000-60. In the C-1000-40 and C-1000-60 groups, the presence of CaO reacted with mixing water and formed $Ca(OH)_2$. The alkalinity provided by $Ca(OH)_2$ promotes the conversion of calcium carbonate to the stable form of calcite during carbonation (Wang et al., 2020). In contrast, in the C-1000-0 and C-1000-20 groups, the slower dissolution of β-C_2S resulted in a lower pH prolonging vaterite stability before its eventual conversion to calcite (Mu et al., 2019).

In the C-1200 group, the calcium silicate phases played a significant role in determining the types of calcium carbonate formed. The crystalline phases included calcite, vaterite, and aragonite, along with residual sand, C_2AS, CS, and C_3S_2. The total $CaCO_3$ content initially decreased to 12.6 % in C-1200-20 and then increased to 19.8 % in C-1200-60. Vaterite content peaked at 11.6 % in C-1200-60, while aragonite content generally decreased from 10.0 % in C-1200-0 to 4.1 % in C-1200-60. This divergence reflects the distinct carbonation behaviors of CS and C_3S_2. Samples dominated by CS (C-1200-0 and C-1200-20) favored aragonite due to the lower pH (<11), limited hydration activity of CS and reduction of Ca^{2+} and OH^- release. In contrast, C_3S_2-rich mixtures (C-1200-40/60) promoted calcite and vaterite formation (Smigelskyte et al., 2020). Post-carbonation, CS content decreased by 8.4 % in C-1200-0 and 20.6 % in C-1200-20, whereas C_3S_2 declined by 23.2 % in C-1200-40 and 27.4 % in C-1200-60. The overall higher reaction rate indicates that increased external calcium carbonate addition in the precursor enhanced the carbonation reaction.

The total generation of $CaCO_3$ varied with activation temperature: 36.9 % (C-800-0), 23.9 % (C-1000-0), and only 14.6 % (C-1200-0). This trend highlights the diminishing carbonation efficiency at elevated temperatures, attributable to the reduced availability of reactive phases such as C_2S, C_3S_2, and CS.

A high-pH, Ca^{2+}-rich pore solution generated by reactive C_2S and/or free CaO (as in the 800 °C and 1000 °C samples) leads to high $CaCO_3$ supersaturation, favoring rapid nucleation and stabilization of calcite as the dominant polymorph (Oral and Ercan, 2018). By contrast, the lower dissolution rates of CS and C_3S_2 in the 1200 °C samples produce a pore solution with reduced Ca^{2+} activity and lower pH, shifting carbonation into a kinetically controlled regime in which metastable polymorphs such as vaterite and aragonite preferentially form and persist (Chang

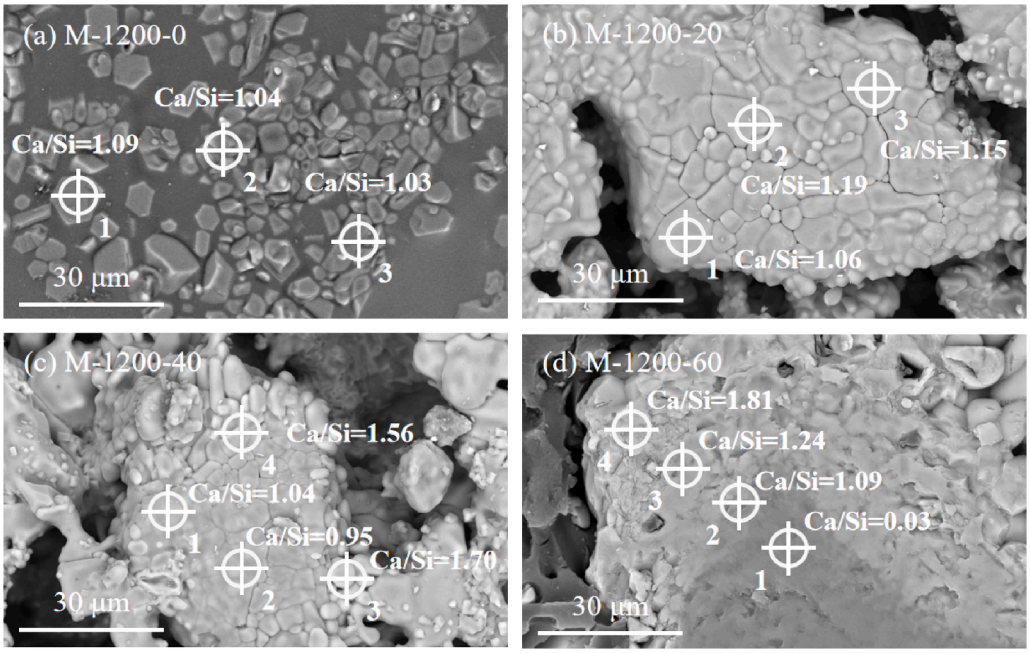

Fig. 12. Morphology of the RCM activated at 1200 °C. (a) M-1200-0, (b) M-1200-20, (c) M-1200-40, and (d) M-1200-60.

et al., 2016; Konopacka-Łyskawa, 2019).

Calcium carbonate content and the carbonation degree are calculated by TGA results. The mass loss between 500 °C and 650 °C is typically attributed to the decomposition of poorly crystallized or metastable forms of calcium carbonate, while mass loss from 650 °C to 850 °C corresponds to the decomposition of well-crystallized calcium carbonate (Ashraf and Olek, 2018b; Goto et al., 1995; Lu et al., 2022; Shen et al., 2022b). The contents of different forms of $CaCO_3$ are quantitatively analyzed using the following equations:

$$CC_{AM}(\%) = \frac{\left(m_{500-650} \times \frac{M_{CaCO_3}}{M_{CO_2}}\right)}{m_{30}} \times 100\% \quad (2)$$

$$CC_{C}(\%) = \frac{\left(m_{650-850} \times \frac{M_{CaCO_3}}{M_{CO_2}}\right)}{m_{30}} \times 100\% \quad (3)$$

where CC_{AM} and CC_C represent the percentages of low and high crystallinity $CaCO_3$, respectively. m_{30} is the initial mass of the samples at room temperature. $m_{500-650}$ and $m_{650-850}$ represent the mass loss within the specified temperature intervals. M_{CaCO_3} and M_{CO_2} are the molecular masses of $CaCO_3$ and CO_2, respectively. The theoretical maximum $CaCO_3$ content is calculated using Eq. (4) and (5). Eq. (6) defines carbonation degree as the ratio of the actual percentage of $CaCO_3$ formed to the theoretical maximum achievable.

$$m_{CO_2max} = 0.785(CaO - 0.7SO_3) + 1.09MgO + 1.42Na_2O + 0.93K_2O \quad (4)$$

$$CC_{max} = m_{CO_2max} \times \frac{M_{CaCO_3}}{M_{CO_2}} \quad (5)$$

$$\text{Carbonation degree} = \frac{CC_{AM} + CC_C}{CC_{max}} \quad (6)$$

where m_{CO_2max} is the theoretical maximum of absorbed CO_2. CC_{max} is the theoretical $CaCO_3$ that can be formed when all calcium phases are carbonated.

The results displayed in Fig. 14 showed that increasing addition of calcium carbonate in the precursors at a certain thermal activation temperature led to an increase in the content of high-crystallinity calcium carbonate ($CaCO_3$). Consequently, both the total $CaCO_3$ generation and the carbonation degree followed a similar upward trend. Conversely, increasing the thermal activation temperature while keeping calcium carbonate addition constant resulted in a significant decrease in both low- and high-crystallinity $CaCO_3$ formation. As a result, the total $CaCO_3$ generated, and the carbonation degree also declined. This is due to higher activation temperatures produce larger amounts of low-calcium silicate phases like CS and C_3S_2 (Ashraf and Olek, 2016), which have a reduced dissolution rate of Ca^{2+} ions (Chang et al., 2016; Ruan et al., 2021). The lower Ca^{2+} concentration weakened the formation of highly crystalline $CaCO_3$ (Ahn et al., 2008), and resulted in a lower decalcification temperatures. This explained why the C-800 and C-1000 series contained a higher content of high-crystallinity $CaCO_3$ (CC_C), while the C-1200 series exhibited lower amounts.

4.4. Porosity and microstructure

The mercury intrusion porosimetry (MIP) results for the carbonated RCM hardened specimens (Fig. 15) illustrated the pore size distribution and porosity for each group. The C-800 group predominantly featured pore sizes between 100 nm and 1 μm and total porosity ranging from 23 % to 29 %, with peak pore sizes at 835 nm, 677 nm, 835 nm, and 349 nm for C-800-0, C-800-20, C-800-40, and C-800-60 respectively. Due to calcium carbonate precipitation filling the pores of carbonated RCM, the variation trend of the peak pore sizes in C-800 group was opposite to that of the calcium carbonate generation amount. The C-1000 group exhibited a wider pore size distribution, ranging from 100 nm to 10 μm and total porosity ranging from 23 % to 31 %, with peaks at 2484 nm, 2053 nm, 834 nm, and 284 nm for C-1000-0, C-1000-20, C-1000-40, and C-1000-60 respectively, suggesting a more porous structure than the C-800 group. Similar to the C-800 group, more calcium carbonate was generated and densified pore structure with the increased participation of sand reaction. The pores of C-1200 group were larger than the previous groups, primarily distributed between 1 μm and 10 μm, with peaks at 2053 nm, 1608 nm, 2818 nm, and 2828 nm for C-1200-0, C-1200-20, C-1200-40, and C-1200-60, respectively. The highest porosity was observed in the C-1200-0 (38 %) and C-1200-20 (37 %) samples, which is attributed to the dominance of low-reactivity CS in these specimens.

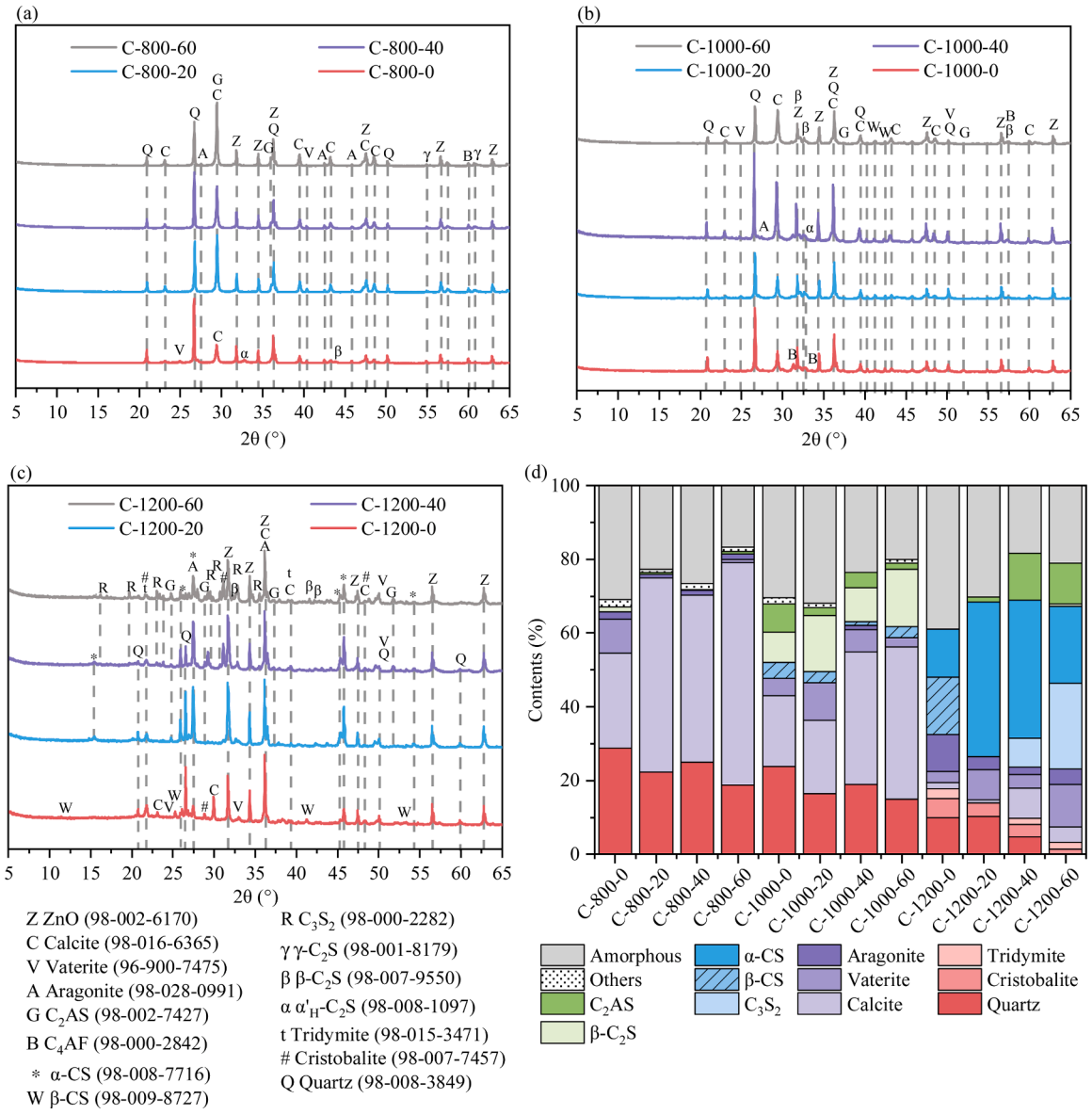

Fig. 13. XRD results of carbonated RCM specimens with preceding activation at (a) 800 °C, (b) 1000 °C, (c) 1200 °C and (d) QXRD results.

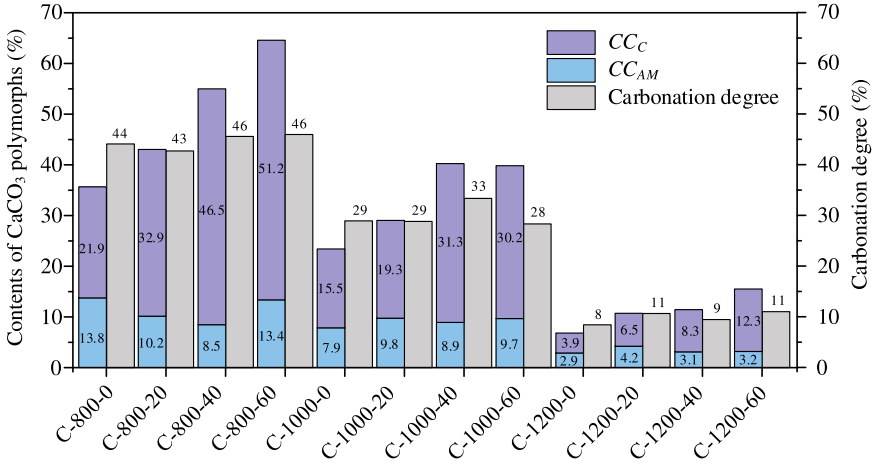

Fig. 14. Calcium carbonate content and the carbonation degree of carbonated RCM specimens.

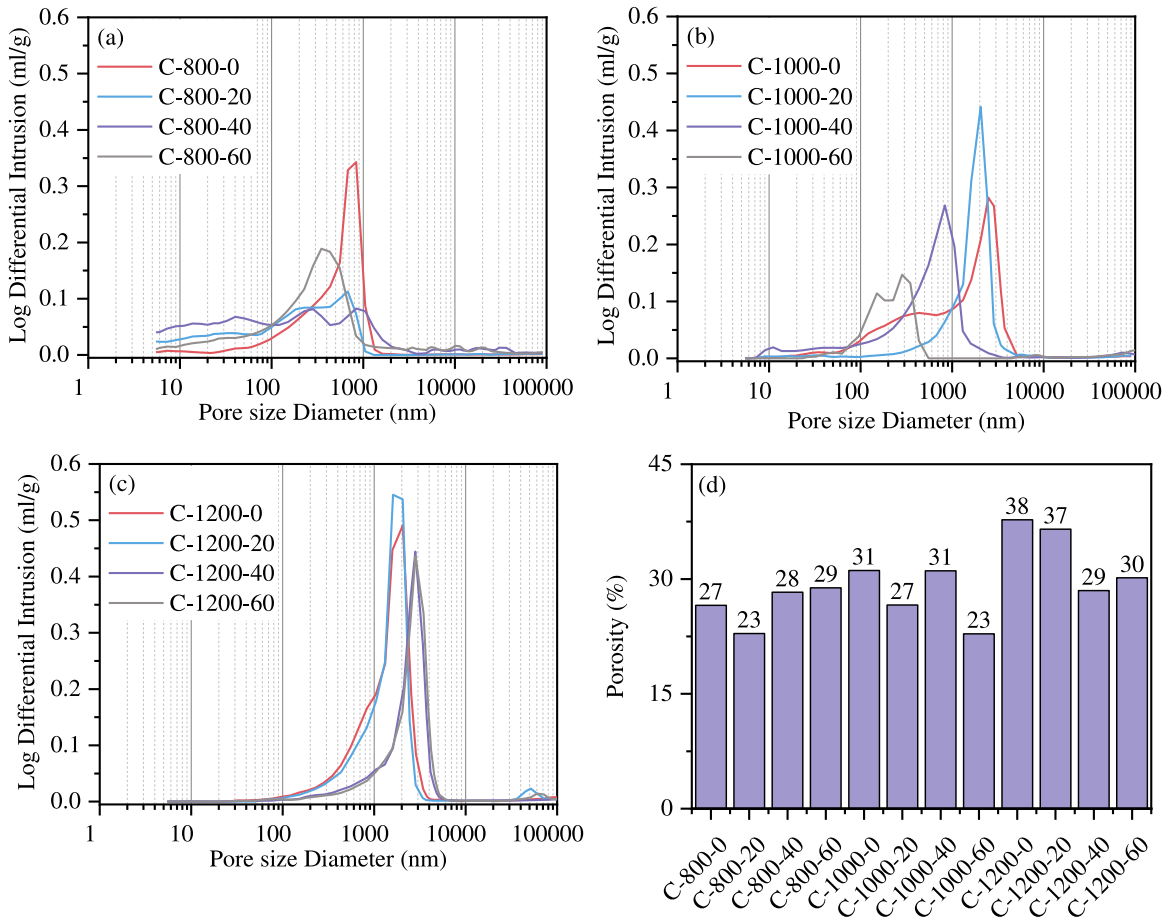

Fig. 15. Pore size distribution of carbonated RCM specimens with preceding activation at (a) 800 °C, (b) 1000 °C, (c) 1200 °C, and (d) porosity.

The lack of amorphous substances failed to fill the voids between crystal particles (Ashraf and Olek, 2016). The C-800 and C-1000 group contained a large amount of C_2S, and generated calcium-modified silica gel to densify their microstructure.

Significant morphological differences were observed among the carbonated RCM specimens (Fig. 16). In the C-800 group (Fig. 16(a)–(d)), vaterite (just presented in C-800-0) and calcite crystals were observed, aligning with the characteristic XRD peaks. This group also contained abundant calcium-modified silica gels. Similarly, the C-1000 group (Fig. 16(e)–(h)) exhibited polymorphs of $CaCO_3$ including calcite, vaterite, and aragonite. The microstructure of the carbonated RCM of C-1000 group revealed a distinct three-layer arrangement: a sand core, an inner layer of C_2S crystals, and an outer shell of $CaCO_3$ polymorphs and calcium-modified silica gel (Fig. 16(f)–(h)). However, the interface between these components appeared loosely bonded in the C-1000-0, likely due to incomplete sand reaction during activation and limited formation of calcium silicate phases. Some C_2S (marked with an orange circle) remained uncarbonated around sand particles. Nonetheless, densely packed rhombohedral calcite crystals were in close contact with C_2S, promoting mechanical interlocking and enhancing the microstructural integrity (Wang et al., 2020). Additionally, calcium-modified silica gel filled voids and bonded mineral phases, further improving local mechanical performance.

In contrast, the C-1200 group (Fig. 16(i)–(l)) showed significant different features. The CS and C_3S_2 phases formed at 1200 °C dissolved and reacted with CO_2 in the pore solution, generating $CaCO_3$ and calcium-modified silica gel (Ashraf et al., 2017; Plattenberger et al., 2018; Smigelskyte et al., 2020). However, the microstructure was composed of loosely packed non-hydraulic minerals (CS and C_3S_2) intermixed with $CaCO_3$ crystals, but lacks amorphous phases like in Fig. 16(a). Vaterite appeared in various morphologies, including spherical, plate-like, and petal-like forms, particularly in the C-1200-60 specimens, as shown in Fig. 16(l). These vaterite forms, along with cubic calcite and rod-like aragonite, contributed to strength through interlocking configurations (Hargis et al., 2024). Nevertheless, the lack of gel-like binding phases likely limited the encapsulation of calcium silicate and carbonate crystals, potentially reducing the overall mechanical performance (Chen and Gao, 2019).

4.5. *Compressive strength of the carbonated specimens*

The compressive strength results for the carbonated RCM specimens (Fig. 17) revealed a clear trend, where RCM activated at 1000 °C generally exhibited superior mechanical performance compared to those activated at 800 °C and 1200 °C.

In the C-800 group, strength development was primarily driven by the formation of cubic calcite crystals during carbonation curing. These crystals contributed mechanical bonding through close packing and interlocking(Wang et al., 2020), with C-800-0 reaching compressive strength at 35.6 MPa. However, the enhancement effect was limited by incomplete decomposition of calcium carbonate during activation, leaving residue $CaCO_3$. Additionally, the low amorphous content meant that many calcite crystals were not encapsulated by binding phases, reducing the overall cohesion and structural integrity.

In contrast, RCM activated at 1000 °C benefited from increased reactivity of sand, which more effectively participated in solid-phase reactions. The presence of calcium carbonate and elevated activation temperature facilitated the formation of calcium silicate phases, which, upon carbonation, yielded $CaCO_3$ and calcium-modified silica gels. These phases contributed to strength gain (De Silva et al., 2006).

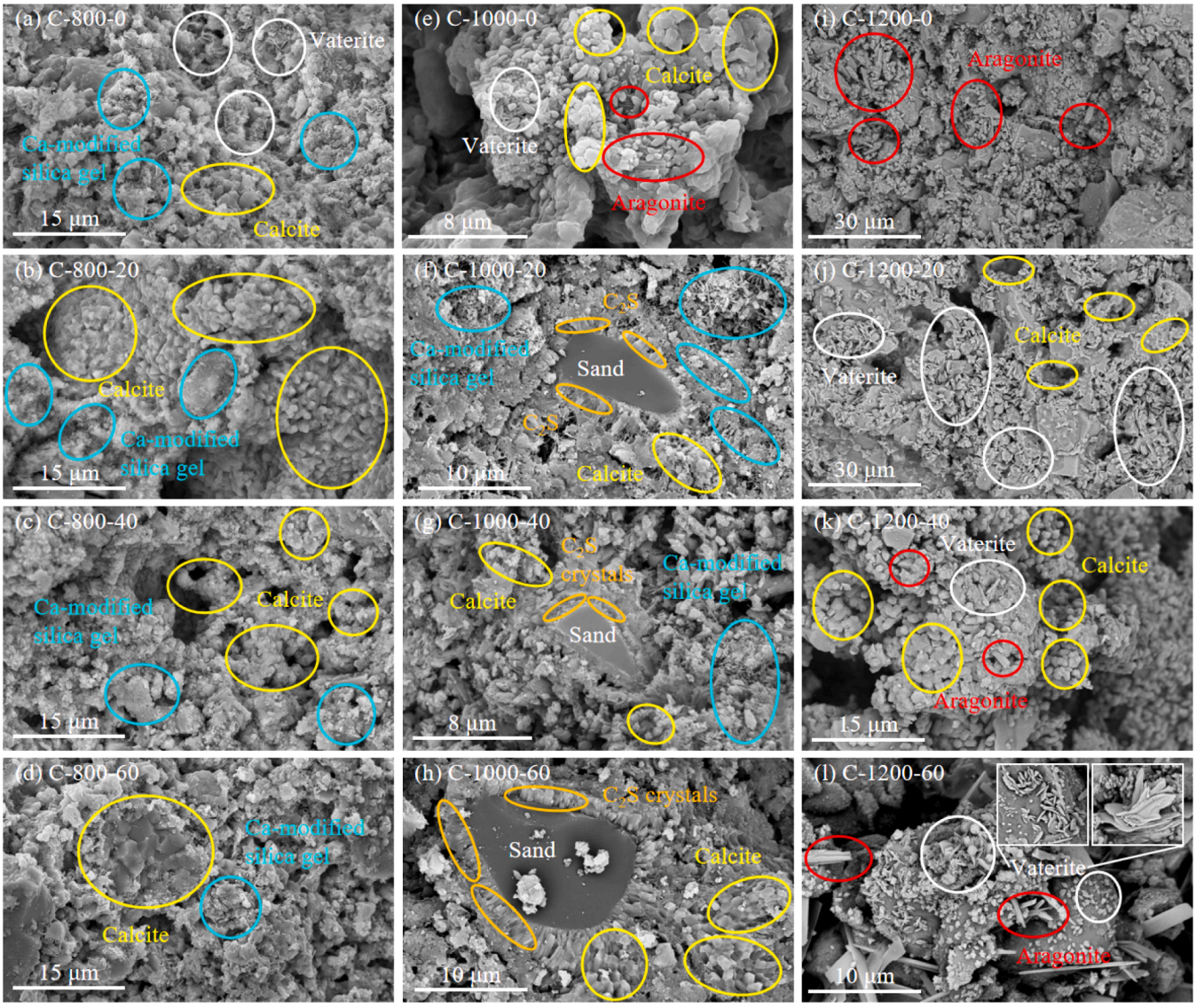

Fig. 16. Morphology of carbonated RCM specimens, labeled sequentially from top to bottom and left to right: (a) C-800-0, (b) C-800-20, (c) C-800-40, (d) C-800-60; (e) C-1000-0, (f) C-1000-20, (g) C-1000-40, (h) C-1000-60; (i) C-1200-0, (j) C-1200-20, (k) C-1200-40, and (l) C-1200-60.

Importantly, the crystallinity of $CaCO_3$, as observed in TGA results (Section 4.3), was found to influence compressive performance. The presence of low-crystallinity $CaCO_3$ and amorphous calcium-modified silica gels was particularly beneficial, underscoring the role of amorphous binding phases in enhancing microstructural densification and strength (Ashraf and Olek, 2018a; Kellermeier et al., 2010; Rostami et al., 2012). As a result, C-1000-20 achieved the highest compressive strength at 36.5 MPa, closely followed by C-1000-0 at 33.2 MPa.

In the C-1200 group, compressive strength increased gradually with calcium carbonate additions, peaking at 12.3 MPa in C-1200-60. The added $CaCO_3$ promoted the formation of calcium silicate phases and improved their Ca/Si ratio, particularly enhancing C_2S formation, which contributed to strength gain. Nevertheless, the overall mechanical performance remained significantly lower than in the C-800-0 and C-1000 group. This reduction was attributed to the dominance of low-reactivity phases such as CS and C_3S_2, which generated fewer carbonation products and resulted in larger pore structures, undermining structural strength.

In summary, the mechanical performance of carbonated RCM specimens is strongly influenced not only by the amount and polymorph type of $CaCO_3$ formed, but also by its crystallinity and morphology. Future studies into the growth models and spatial distribution of $CaCO_3$ crystals may yield further insights for optimizing mechanical properties in RCM systems.

4.6. CO_2 emissions of the RCM

The life-cycle inventory was compiled using Ecoinvent v3.9 datasets implemented in SimaPro. The system boundary was cradle-to-gate, encompassing the production of 1 tonne of cured cementitious paste as the functional unit. This enables a comparison between carbonation-cured RCM and conventionally water-cured ordinary Portland cement (OPC), the latter serving as the baseline for current industry practice. Three high-performance RCM formulations (C-800-0, C-1000-0, and C-1000-20) were selected for analysis.

For the OPC benchmark, the system boundary encompassed raw material extraction, calcination, grinding, mixing, and water curing. For RCM, the boundaries included raw material sourcing (limestone, superplasticizer), thermal activation, grinding, mixing, and carbonation curing. Recycled concrete fines (RCF) were assumed to be pre-collected, with a 50 km transport distance to the processing site. The CO_2 used for curing was modeled as on-site recovered flue gas, avoiding

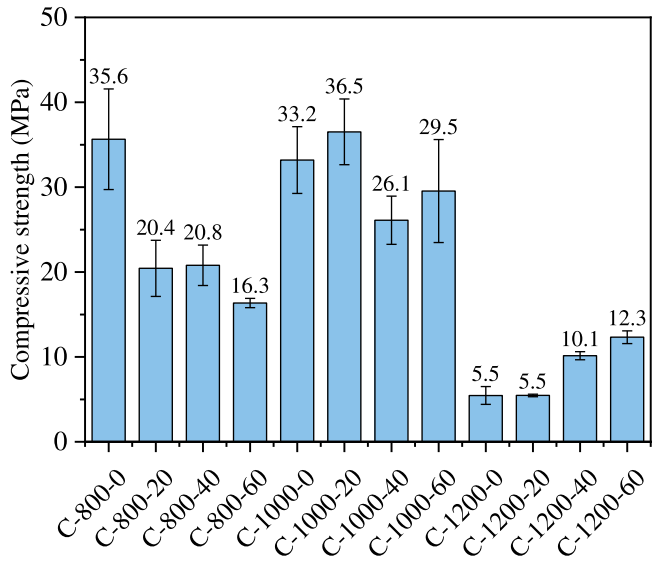

Fig. 17. Compressive strength of carbonated RCM specimens.

transportation emissions. Furthermore, the impacts of cement kiln retrofitting were excluded from the analysis. Key assumptions for thermal activation energy (scaled by activation temperature), electricity mix (CH grid), transport distance (50 tkm), and CO_2 uptake (derived directly from TGA measurements) are summarized in Table S2 of the Supplementary Material. A comprehensive depiction of system boundaries and LCA results was shown in Fig. 18.

The results demonstrated substantial carbon reduction potential: total GWP values were 99, 155, and 231 kg CO_2 eq/t for the C-800-0, C-1000-0, and C-1000-20 groups, respectively. These correspond to reductions of 83 %, 74 %, and 61 %, relative to OPC (591 kg CO_2 eq/t). The reductions arise from two primary mechanisms: (i) substituting limestone with RCF eliminates large scale limestone decomposition during clinkering of OPC (limestone serves as additives in this study), (ii) carbonation curing directly sequesters CO_2 through mineral formation, partially offsetting emissions from the thermal activation process. These findings demonstrate that carbonation-cured RCM offers a viable and scalable pathway for low-carbon cement production, particularly in regions with abundant concrete waste and access to CO_2-rich industrial emissions.

5. Conclusion

This study demonstrated that modulating the calcium-to-silicon (Ca/Si) ratio and applying thermal activation effectively enhanced the reactivity of sand particles in recycled concrete fines, enabling the production of reactivated cementitious materials and promoting the sustainable reuse of waste concrete. Comprehensive analyses of morphological evolution, phase assemblage, carbonation products, microstructure, and compressive strength were conducted using XRD, TGA, MIP, SEM, and mechanical testing. The key findings are summarized below:

1) The composition of calcium silicate minerals in RCM evolved significantly with activation temperature. At 800 °C, α'_H-C_2S and β-C_2S were predominant. At 1000 °C, α'_H-C_2S disappeared, leaving β-C_2S as the dominant phase. At 1200 °C, silicate phases transformed into low-reactivity CS or C_3S_2, indicating over-sintering and reduced hydraulic potential.

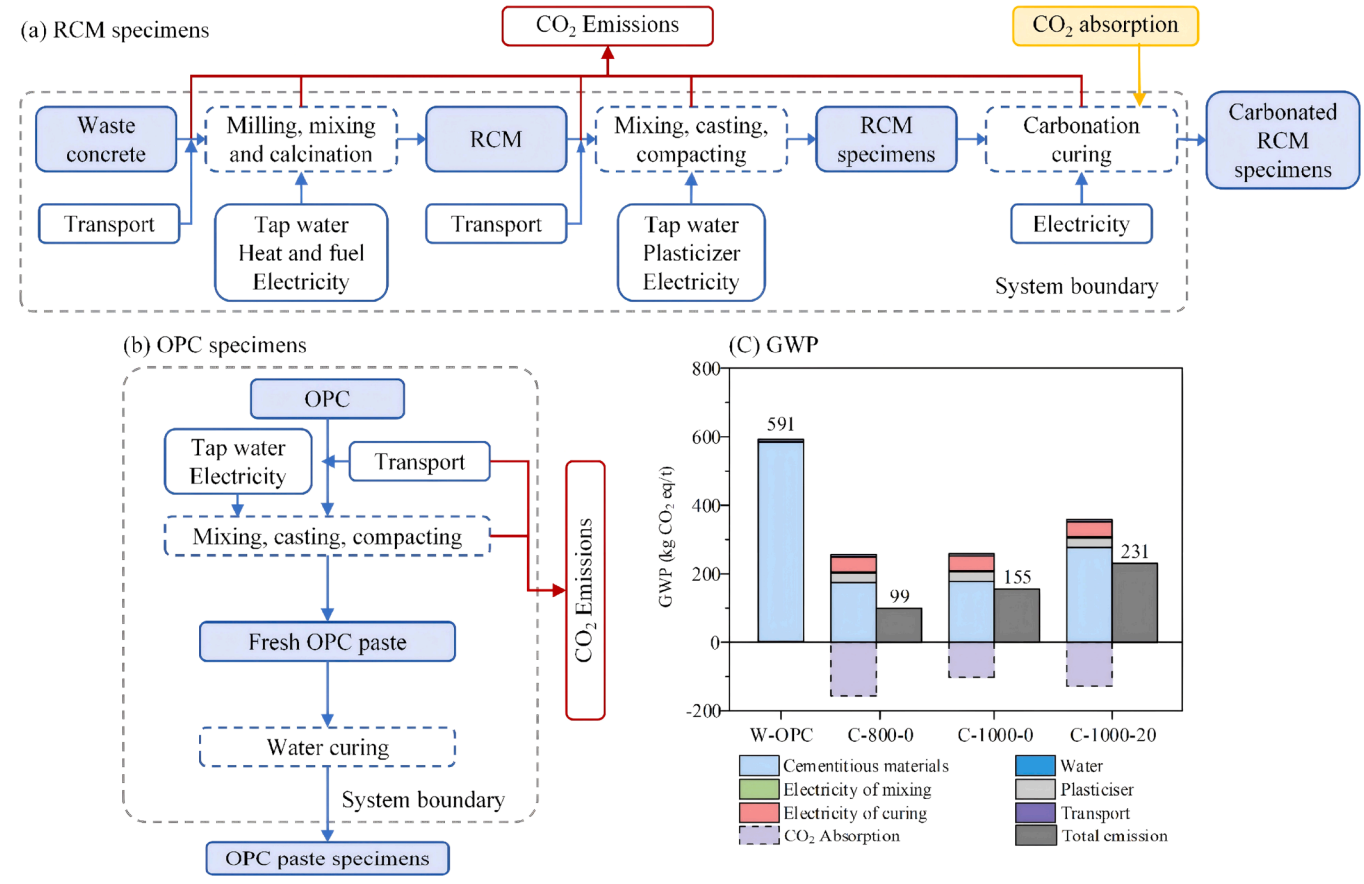

Fig. 18. The system boundaries of (a) RCM and (b) OPC specimens. The (c) GWP results.

2) Adjusting the Ca/Si ratio enhanced the reaction of sand, particularly at higher activation temperatures. At 800 °C, substantial unreacted $CaCO_3$ and sand remained, suggesting limited impact. At 1000 °C, Ca/Si modulation significantly increased C_2S formation and reduced sand content. At 1200 °C, $CaCO_3$ addition further promoted quartz transformation into cristobalite and tridymite, and increased the Ca/Si ratio in resulting silicate minerals.
3) Activation temperature strongly influenced the type and amount of $CaCO_3$ polymorphs in carbonated RCM. Calcite was the main product at 800 °C and 1000 °C, correlating with higher compressive strength. At 1200 °C, calcite formation declined sharply, leading to reduced total $CaCO_3$ content. In the absence of $CaCO_3$ addition, compressive strength declined with increasing activation temperature, due to the lack of amorphous $CaCO_3$ and calcium-modified silica gel. The highest strength (36.5 MPa) was observed in C-1000-20. When $CaCO_3$ was added, RCM activated at 1000 °C delivered the best overall mechanical performance. Furthermore, carbonation-cured RCM specimens achieved up to 61 % reduction in CO_2 emissions compared to OPC, confirming their promise as low-carbon alternatives.

In conclusion, this research confirms the potential of thermal activation combined with Ca/Si ratio control for converting RCF into low-carbon cementitious materials. The approach reduces dependence on natural limestone while enabling CO_2 sequestration.

Future implementation of waste concrete recycling based on thermally activated RCF depends on several key advances. The thermal activation process must be scaled by leveraging existing cement kiln infrastructure, which requires systematic evaluation of the compatibility of RCF with standard kiln feed and its potential impact on clinker quality, energy efficiency, and emissions. An economic and environmental comparison of alternative calcium sources is also required, including the use of industrial by-products as substitutes for natural limestone. Most critically, robust strategies must be developed to manage the highly variable composition present in real-world RCF streams, arising from differences in cement type, supplementary cementitious materials, and service exposure. Overcoming these challenges is essential to transition the proposed technology from laboratory-scale validation to a viable circular solution for the construction industry.

CRediT authorship contribution statement

Yutong Ju: Writing – original draft, Visualization, Validation, Investigation. **Ye Li:** Writing – review & editing, Supervision, Resources, Methodology, Formal analysis, Conceptualization. **Xiangping Xian:** Writing – review & editing, Supervision, Resources, Formal analysis. **Tiejun Liu:** Validation, Resources, Project administration, Data curation, Conceptualization.

Declaration of competing interest

The authors declare that they have no known competing financial interests or personal relationships that could have appeared to influence the work reported in this paper.

Acknowledgments

This work was supported by the National Science Fund for Distinguished Young Scholars (No. 52025081), the National Natural Science Foundation of China (U23A20658, 52378229), Science and Technology Planning Project of Guangdong Province (2023A0505050098), and the Faculty Start-up Grant of City University of Hong Kong (9610660).

Supplementary materials

Supplementary material associated with this article can be found, in the online version, at doi:10.1016/j.ccst.2025.100557.

References

Abo-Almaged, H.H., Ngida, R.E.A., Ajiba, N.A., Sadek, H.E.H., Khattab, R.M., 2024. Utilization of industrial waste materials for the preparation of wollastonite by temperature-induced forming technique. Sci. Rep. 14 (1), 21752. https://doi.org/10.1038/s41598-024-71243-3.

Ahn, J.W., Choi, K.S., Yoon, S.H., Kim, H., 2008. Synthesis of Aragonite by the carbonation process. J. Am. Ceram. Soc. 87 (2), 286–288. https://doi.org/10.1111/j.1551-2916.2004.00286.x.

Alarcon-Ruiz, L., Platret, G., Massieu, E., Ehrlacher, A., 2005. The use of thermal analysis in assessing the effect of temperature on a cement paste. Cem. Concr. Res. 35 (3), 609–613. https://doi.org/10.1016/j.cemconres.2004.06.015.

Alonso, C., Fernandez, L., 2004. Dehydration and rehydration processes of cement paste exposed to high temperature environments. J. Mater. Sci. 39 (9), 3015–3024. https://doi.org/10.1023/B:JMSC.0000025827.65956.18.

Amiri, M., Aryanpour, M., Porhonar, F., 2022. Microstructural study of concrete performance after exposure to elevated temperatures via considering C–S–H nanostructure changes. High Temper. Mater. Processes 41 (1), 224–237.

Ashraf, W., Olek, J., 2016. Carbonation behavior of hydraulic and non-hydraulic calcium silicates: potential of utilizing low-lime calcium silicates in cement-based materials. J. Mater. Sci. 51 (13), 6173–6191. https://doi.org/10.1007/s10853-016-9909-4.

Ashraf, W., Olek, J., 2018a. Carbonation activated binders from pure calcium silicates: reaction kinetics and performance controlling factors. Cem. Concr. Compos. 93, 85–98. https://doi.org/10.1016/j.cemconcomp.2018.07.004.

Ashraf, W., Olek, J., 2018b. Elucidating the accelerated carbonation products of calcium silicates using multi-technique approach. J. CO2. Util. 23, 61–74. https://doi.org/10.1016/j.jcou.2017.11.003.

Ashraf, W., Olek, J., Jain, J., 2017. Microscopic features of non-hydraulic calcium silicate cement paste and mortar. Cem. Concr. Res. 100, 361–372. https://doi.org/10.1016/j.cemconres.2017.07.001.

Autef, A., Joussein, E., Gasgnier, G., Rossignol, S., 2012. Role of the silica source on the geopolymerization rate. J. Non. Cryst. Solids. 358 (21), 2886–2893. https://doi.org/10.1016/j.jnoncrysol.2012.07.015.

Ávalos-Rendón, T.L., Chelala, E.A.P., Mendoza Escobedo, C.J., Figueroa, I.A., Lara, V.H., Palacios-Romero, L.M., 2018. Synthesis of belite cements at low temperature from Silica fume and natural commercial zeolite. Mater. Sci. Eng.: B 229, 79–85. https://doi.org/10.1016/j.mseb.2017.12.020.

Beaudoin, J., Odler, I., 2019. 5 - Hydration, setting and hardening of Portland cement. In: Hewlett, P.C., Liska, M. (Eds.), Lea's Chemistry of Cement and Concrete, 5th Edition. Butterworth-Heinemann, pp. 157–250. https://doi.org/10.1016/B978-0-08-100773-0.00005-8.

Bogas, J.A., Carriço, A., Pereira, M.F.C., 2019. Mechanical characterization of thermal activated low-carbon recycled cement mortars. J. Clean. Prod. 218, 377–389. https://doi.org/10.1016/j.jclepro.2019.01.325.

Bogas, J.A., Carriço, A., Tenza-Abril, A.J., 2020. Microstructure of thermoactivated recycled cement pastes. Cem. Concr. Res. 138. https://doi.org/10.1016/j.cemconres.2020.106226.

Brahimi, A., Meghachou, M., Abbad, H., Rahmouni, A., Belbachir, M., 2020. Valorization of raw materials based on fly ash of eggshells and Algerian sand dune (Southern West of Algeria) for synthesis of environmentally cementitious materials: synthesis and characterization. Geotech. Geol. Eng. (Dordr) 42 (1), 687–702. https://doi.org/10.1007/s10706-020-01598-7.

Bullard, J.W., Jennings, H.M., Livingston, R.A., Nonat, A., Scherer, G.W., Schweitzer, J. S., Scrivener, K.L., Thomas, J.J., 2011. Mechanisms of cement hydration. Cem. Concr. Res. 41 (12), 1208–1223. https://doi.org/10.1016/j.cemconres.2010.09.011.

Cai, Y., Xuan, D., Hou, P., Shi, J., Poon, C.S., 2021. Effect of seawater as mixing water on the hydration behaviour of tricalcium aluminate. Cem. Concr. Res. 149. https://doi.org/10.1016/j.cemconres.2021.106565.

Carriço, A., Real, S., Bogas, J.A., Costa Pereira, M.F., 2020. Mortars with Thermo activated recycled cement: fresh and mechanical characterisation. Constr. Build. Mater. 256. https://doi.org/10.1016/j.conbuildmat.2020.119502.

Chang, R., Choi, D., Kim, M.H., Park, Y., 2016. Tuning crystal polymorphisms and structural investigation of precipitated calcium carbonates for CO_2 mineralization. ACS. Sustain. Chem. Eng. 5 (2), 1659–1667. https://doi.org/10.1021/acssuschemeng.6b02411.

Chen, T., Gao, X., 2019. Effect of carbonation curing regime on strength and microstructure of Portland cement paste. J. CO2. Util. 34, 74–86. https://doi.org/10.1016/j.jcou.2019.05.034.

Crook, D.N., Murray, M.J., 1970. Regain of strength after firing of concrete. Magazine Concrete Res. 22 (72), 149–154. https://doi.org/10.1680/macr.1970.22.72.149.

De Silva, P., Bucea, L., Moorehead, D.R., Sirivivatnanon, V., 2006. Carbonate binders: reaction kinetics, strength and microstructure. Cem. Concr. Compos. 28 (7), 613–620. https://doi.org/10.1016/j.cemconcomp.2006.03.004.

Duan, H., Li, J., 2016. Construction and demolition waste management: china's lessons. Waste Manag. Res. 34 (5), 397–398. https://doi.org/10.1177/0734242X16647603.

Fang, Z., Xiong, G., Shao, Z., Zhou, S., Ou, G., Liu, L., Suzuki, M., Wang, C., Sakai, Y., 2024. Electrochemical recycling of recycled concrete powder: selective recovery of calcium and silica to enable sustainable construction materials. Resources, Environ. Sustain. 18. https://doi.org/10.1016/j.resenv.2024.100182.

Ge, P., Chen, X., Wu, Y., Quan, J., Yan, Y., Li, M., Zhou, J., Liu, B., 2025. A method for separating gravel aggregates, sand and hardened cement by high-temperature heating, ball milling and sieving. Constr. Build. Mater. 466. https://doi.org/10.1016/j.conbuildmat.2025.140300.

Goto, S., Suenaga, K., Kado, T., Fukuhara, M., 1995. Calcium silicate carbonation products. J. Am. Ceram. Soc. 78 (11), 2867–2872. https://doi.org/10.1111/j.1151-2916.1995.tb09057.x.

Handoo, S.K., Agarwal, S., Agarwal, S.K., 2002. Physicochemical, mineralogical, and morphological characteristics of concrete exposed to elevated temperatures. Cem. Concr. Res. 32 (7), 1009–1018. https://doi.org/10.1016/S0008-8846(01)00736-0.

Hargis, C.W., Chen, I., Wang, Y., Maraghechi, H., Gilliam, R.J., Monteiro, P.J.M., 2024. Microstructure development of calcium carbonate cement through polymorphic transformations. Cem. Concr. Compos. 153. https://doi.org/10.1016/j.cemconcomp.2024.105715.

Infante Gomes, R., Brazão Farinha, C., Veiga, R., de Brito, J., Faria, P., Bastos, D., 2021. CO_2 sequestration by construction and demolition waste aggregates and effect on mortars and concrete performance - an overview. Renewable and Sustainable Energy Reviews 152. https://doi.org/10.1016/j.rser.2021.111668.

Ji, G., Peng, X., Wang, S., Li, J., Sun, K., Chi, H., 2024. Influence of ground quartz sand finesses on the formation of poorly ordered calcium silicate hydrate prepared by dynamically hydrothermal synthesis. Case Studies Constr. Mater. 20. https://doi.org/10.1016/j.cscm.2023.e02746.

Kalinowska-Wichrowska, K., Kosior-Kazberuk, M., Pawluczuk, E., 2019. The properties of composites with recycled cement mortar used as a supplementary cementitious material. Materials. (Basel) 13 (1). https://doi.org/10.3390/ma13010064.

Kellermeier, M., Melero-García, E., Glaab, F., Klein, R., Drechsler, M., Rachel, R., García-Ruiz, J.M., Kunz, W., 2010. Stabilization of amorphous calcium carbonate in inorganic silica-rich environments. J. Am. Chem. Soc. 132 (50), 17859–17866. https://doi.org/10.1021/ja106959p.

Konopacka-Łyskawa, D., 2019. Synthesis methods and favorable conditions for spherical vaterite precipitation: a review. Crystals. (Basel) 9 (4), 223.

Lee, N.K., Koh, K.T., An, G.H., Ryu, G.S., 2017a. Influence of binder composition on the gel structure in alkali activated fly ash/slag pastes exposed to elevated temperatures. Ceram. Int. 43 (2), 2471–2480. https://doi.org/10.1016/j.ceramint.2016.11.042.

Lee, N.K., Koh, K.T., Park, S.H., Ryu, G.S., 2017b. Microstructural investigation of calcium aluminate cement-based ultra-high performance concrete (UHPC) exposed to high temperatures. Cem. Concr. Res. 102, 109–118. https://doi.org/10.1016/j.cemconres.2017.09.004.

Li, Y., Han, D., Wang, H., Lyu, H., Zou, D., liu, T., 2023. Carbonation curing of mortars produced with reactivated cementitious materials for CO_2 sequestration. J. Clean. Prod. 383. https://doi.org/10.1016/j.jclepro.2022.135501.

Li, Y., Mi, T., Liu, W., Dong, Z., Dong, B., Tang, L., Xing, F., 2021. Chemical and mineralogical characteristics of carbonated and uncarbonated cement pastes subjected to high temperatures. Composites Part B: Engineering 216. https://doi.org/10.1016/j.compositesb.2021.108861.

Liao, H., Ju, Y., Lyu, H., Liu, T., Han, D., Li, Y., 2024. Compressive strength development and microstructure evolution of mortars prepared using reactivated cementitious materials under carbonation curing. Developm. Built Environ. 18. https://doi.org/10.1016/j.dibe.2024.100397.

Liu, K., Ouyang, J., Sun, D., Jiang, N., Wang, A., Huang, N., Liang, P., 2022. Enhancement mechanism of different recycled fine aggregates by microbial induced carbonate precipitation. J. Clean. Prod. 379. https://doi.org/10.1016/j.jclepro.2022.134783.

Lu, B., Drissi, S., Liu, J., Hu, X., Song, B., Shi, C., 2022. Effect of temperature on CO_2 curing, compressive strength and microstructure of cement paste. Cem. Concr. Res. 157. https://doi.org/10.1016/j.cemconres.2022.106827.

Lu, B., He, P., Liu, J., Peng, Z., Song, B., Hu, X., 2021. Microstructure of Portland cement paste subjected to different CO_2 concentrations and further water curing. J. CO2. Util. 53, 101714. https://doi.org/10.1016/j.jcou.2021.101714.

Luo, W., Shi, Z., Wang, W., Liu, Z., Liu, Z., 2025. Study of phase transformation of calcium silicate using desert sand as raw materials. Int. J. Appl. Ceram. Technol. 22 (2), e14984. https://doi.org/10.1111/ijac.14984.

Mao, Y., Drissi, S., He, P., Hu, X., Zhang, J., Shi, C., 2024a. Quantifying the effects of wet carbonated recycled cement paste powder on the properties of cement paste. Cem. Concr. Res. 175. https://doi.org/10.1016/j.cemconres.2023.107381.

Mao, Y., Hu, X., Alengaram, U.J., Chen, W., Shi, C., 2024b. Use of carbonated recycled cement paste powder as a new supplementary cementitious material: a critical review. Cem. Concr. Compos. 154. https://doi.org/10.1016/j.cemconcomp.2024.105783.

Miller, S.A., Horvath, A., Monteiro, P.J.M., 2016. Readily implementable techniques can cut annual CO_2 emissions from the production of concrete by over 20%. Environ. Rese. Letters 11 (7), 074029–074036. https://doi.org/10.1088/1748-9326/11/7/074029.

Mu, Y., Liu, Z., Wang, F., 2019. Comparative study on the carbonation-activated calcium silicates as sustainable binders: reactivity, mechanical performance, and microstructure. ACS. Sustain. Chem. Eng. 7 (7), 7058–7070. https://doi.org/10.1021/acssuschemeng.8b06841.

Mucsi, G., Halyag Papné, N., Ulsen, C., Figueiredo, P.O., Kristály, F., 2021. Mechanical activation of construction and demolition waste in order to improve its Pozzolanic reactivity. ACS. Sustain. Chem. Eng. 9 (9), 3416–3427. https://doi.org/10.1021/acssuschemeng.0c05838.

Okada, Y., Sasaki, K., Zhong, B., Ishida, H., Mitsuda, T., 2005. Formation processes of β-C_2S by the decomposition of hydrothermally prepared C-S-H with $Ca(OH)_2$. J. Am. Ceram. Soc. 77, 1319–1323. https://doi.org/10.1111/j.1151-2916.1994.tb05409.x.

Oral, Ç.M., Ercan, B., 2018. Influence of pH on morphology, size and polymorph of room temperature synthesized calcium carbonate particles. Powder. Technol. 339, 781–788. https://doi.org/10.1016/j.powtec.2018.08.066.

Pagliari, L., Dapiaggi, M., Pavese, A., Francescon, F., 2013. A kinetic study of the quartz-cristobalite phase transition. J. Eur. Ceram. Soc. 33 (15–16), 3403–3410. https://doi.org/10.1016/j.jeurceramsoc.2013.06.014.

Peng, G.-F., Huang, Z.-S., 2008. Change in microstructure of hardened cement paste subjected to elevated temperatures. Constr. Build. Mater. 22 (4), 593–599. https://doi.org/10.1016/j.conbuildmat.2006.11.002.

Plattenberger, D.A., Ling, F.T., Tao, Z., Peters, C.A., Clarens, A.F., 2018. Calcium silicate crystal structure impacts reactivity with CO_2 and precipitate chemistry. Environ. Sci. Technol. Lett. 5 (9), 558–563. https://doi.org/10.1021/acs.estlett.8b00386.

Pristerà, G., Tonini, D., Lamperti Tornaghi, M., Caro, D., Sala, S., 2024. Taxonomy of design for deconstruction options to enable circular economy in buildings. Resources, Environment and Sustainability 15. https://doi.org/10.1016/j.resenv.2024.100153.

Ram, V.G., Kishore, K.C., Kalidindi, S.N., 2020. Environmental benefits of construction and demolition debris recycling: evidence from an Indian case study using life cycle assessment. J. Clean. Prod. 255. https://doi.org/10.1016/j.jclepro.2020.120258.

Real, S., Carriço, A., Bogas, J.A., Guedes, M., 2020. Influence of the treatment temperature on the microstructure and hydration behavior of thermoactivated recycled cement. Materials. (Basel) 13 (18), 3937.

Ren, M., Shen, P., Jiang, Y., He, J., Qin, Q., Poon, C.-s., 2025. Insights into the carbonation behavior of polymorphs of Ca2SiO4 (C2S): the role of calcination temperature. Cem. Concr. Res. 198, 108005. https://doi.org/10.1016/j.cemconres.2025.108005.

Rostami, V., Shao, Y., Boyd, A.J., He, Z., 2012. Microstructure of cement paste subject to early carbonation curing. Cem. Concr. Res. 42 (1), 186–193. https://doi.org/10.1016/j.cemconres.2011.09.010.

Ruan, F., Kawanishi, S., Sukenaga, S., Shibata, H., 2021. Effect of the silicate skeleton structure on the dissolution kinetics of calcium silicate mineral phases in water. Metallurg. Mater. Trans. B 52 (2), 1071–1084. https://doi.org/10.1007/s11663-021-02079-9.

Saeki, N., Cheng, L., Kurihara, R., Ohkubo, T., Teramoto, A., Suda, Y., Kitagaki, R., Maruyama, I., 2024. Natural carbonation process in cement paste particles in different relative humidities. Cem. Concr. Compos. 146, 105400. https://doi.org/10.1016/j.cemconcomp.2023.105400.

Serpell, R., Lopez, M., 2013. Reactivated cementitious materials from hydrated cement paste wastes. Cem. Concr. Compos. 39, 104–114. https://doi.org/10.1016/j.cemconcomp.2013.03.020.

Serpell, R., Lopez, M., 2015. Properties of mortars produced with reactivated cementitious materials. Cem. Concr. Compos. 64, 16–26. https://doi.org/10.1016/j.cemconcomp.2015.08.003.

Serpell, R., Zunino, F., 2017. Recycling of hydrated cement pastes by synthesis of α'_H-C_2S. Cem. Concr. Res. 100, 398–412. https://doi.org/10.1016/j.cemconres.2017.08.001.

Shen, P., Lu, J., Zhang, Y., Jiang, Y., Zhang, S., Poon, C.S., 2022a. Preparation aragonite whisker-rich materials by wet carbonation of cement: towards yielding micro-fiber reinforced cement and sequestrating CO2. Cem. Concr. Res. 159. https://doi.org/10.1016/j.cemconres.2022.106891.

Shen, P., Zhang, Y., Jiang, Y., Zhan, B., Lu, J., Zhang, S., Xuan, D., Poon, C.S., 2022b. Phase assemblance evolution during wet carbonation of recycled concrete fines. Cem. Concr. Res. 154. https://doi.org/10.1016/j.cemconres.2022.106733.

Shui, Z., Xuan, D., Chen, W., Yu, R., Zhang, R., 2009. Cementitious characteristics of hydrated cement paste subjected to various dehydration temperatures. Constr. Build. Mater. 23 (1), 531–537. https://doi.org/10.1016/j.conbuildmat.2007.10.016.

Shui, Z., Xuan, D., Wan, H., Cao, B., 2008. Rehydration reactivity of recycled mortar from concrete waste experienced to thermal treatment. Constr. Build. Mater. 22 (8), 1723–1729. https://doi.org/10.1016/j.conbuildmat.2007.05.012.

Smigelskyte, A., Siauciunas, R., Hilbig, H., Decker, M., Urbonas, L., Skripkiunas, G., 2020. Carbonated rankinite binder: effect of curing parameters on microstructure, strength development and durability performance. Sci. Rep. 10 (1). https://doi.org/10.1038/s41598-020-71270-w.

Sun, F., Pang, X., Wei, J., Matschei, T., Sun, L., Yu, Y., Wang, H., Sun, J., 2024. Stability of calcium silicate hydrates produced by alite hydration at high and ultrahigh temperatures. Cem. Concr. Res. 179. https://doi.org/10.1016/j.cemconres.2024.107469.

Tang, Q., Ma, Z., Wu, H., Wang, W., 2020. The utilization of eco-friendly recycled powder from concrete and brick waste in new concrete: a critical review. Cem. Concr. Compos. 114. https://doi.org/10.1016/j.cemconcomp.2020.103807.

Termkhajornkit, P., Barbarulo, R., Chanvillard, G., 2015. Microstructurally-designed cement pastes: a mimic strategy to determine the relationships between microstructure and properties at any hydration degree. Cem. Concr. Res. 71, 66–77. https://doi.org/10.1016/j.cemconres.2015.01.020.

Trník, A., Fořt, J., Pavlíková, M., Čáchová, M., Čítek, D., Kolísko, J., Černý, R., Pavlík, Z., 2016. UHPFRC at high temperatures–Simultaneous thermal analysis and thermodilatometry. In: AIP Conference proceedings. AIP Publishing.

Viggh, E., Eriksson, M., Wilhelmsson, B., Backman, R., 2020. Early formation of belite in cement clinker raw materials with slag. Adv. Cement Res. 33 (6), 249–256. https://doi.org/10.1680/jadcr.19.00150.

Wang, D., Xiong, C., Li, W., Chang, J., 2020. Growth of calcium carbonate induced by accelerated carbonation of tricalcium silicate. ACS. Sustain. Chem. Eng. 8 (39), 14718–14731. https://doi.org/10.1021/acssuschemeng.0c02260.

Wang, J., Mu, M., Liu, Y., 2018. Recycled cement. Constr. Build. Mater. 190, 1124–1132. https://doi.org/10.1016/j.conbuildmat.2018.09.181.

Wang, X., Guo, M.-Z., Ling, T.-C., 2022. Review on CO_2 curing of non-hydraulic calcium silicates cements: mechanism, carbonation and performance. Cem. Concr. Compos. 133. https://doi.org/10.1016/j.cemconcomp.2022.104641.

Wong, H.S., Buenfeld, N.R., 2009. Determining the water–cement ratio, cement content, water content and degree of hydration of hardened cement paste: method development and validation on paste samples. Cem. Concr. Res. 39 (10), 957–965. https://doi.org/10.1016/j.cemconres.2009.06.013.

Xi, X., Zheng, Y., Du, C., Zhang, P., Sun, M., 2024. Study on the hydration characteristics, mechanical properties, and microstructure of thermally activated low-carbon recycled cement. Constr. Build. Mater. 447. https://doi.org/10.1016/j.conbuildmat.2024.138042.

Xu, L., Wang, J., Li, K., Li, M., Lin, S., Hao, T., Wang, T., Guo, Y., Ling, Z., 2023. Investigations on the rehydration of recycled blended SCMs cement. Cem. Concr. Res. 163. https://doi.org/10.1016/j.cemconres.2022.107036.

Xu, L., Wang, J., Li, K., Lin, S., Li, M., Hao, T., Ling, Z., Xiang, D., Wang, T., 2022. A systematic review of factors affecting properties of thermal-activated recycled cement. Resources. Conservation and Recycling 185. https://doi.org/10.1016/j.resconrec.2022.106432.

Xu, Y., Song, P., Cao, W.G., Li, H., Liang, J.L., 2021. Effect of Al_2O_3-SiO_2 addition on gehlenite growth and the mechanical performance of steel slag. Crystals. (Basel) 11 (8). https://doi.org/10.3390/cryst11080936.

Zanovello, M., John, V.M., White, C.E., Angulo, S.C., 2024. Engineered blended thermoactivated recycled cement: a study on reactivity, water demand, strength-porosity, and CO2 emissions. ACS. Sustain. Chem. Eng. 13 (2), 800–814. https://doi.org/10.1021/acssuschemeng.4c06567.

Zhao, D., Williams, J.M., Hou, P., Moment, A.J., Kawashima, S., 2024. Stabilizing mechanisms of metastable vaterite in cement systems. Cem. Concr. Res. 178. https://doi.org/10.1016/j.cemconres.2024.107441.

Zhao, S., Liu, Z., Wang, F., Hu, S., Liu, C., 2021. Effect of extended carbonation curing on the properties of γ-C2S compacts and its implications on the multi-step reaction mechanism. ACS. Sustain. Chem. Eng. 9 (19), 6673–6684. https://doi.org/10.1021/acssuschemeng.1c00200.

Zheng, Q., Jiang, J., Li, X., Bustillo, K.C., Zheng, H., 2021. In situ TEM observation of calcium silicate hydrate nanostructure at high temperatures. Cem. Concr. Res. 149. https://doi.org/10.1016/j.cemconres.2021.106579.

Zhu, C., Fang, Y., Wei, H., 2018. Carbonation-cementation of recycled hardened cement paste powder. Constr. Build. Mater. 192, 224–232. https://doi.org/10.1016/j.conbuildmat.2018.10.113.

Zhutovsky, S., Shishkin, A., 2021. Recycling of hydrated Portland cement paste into new clinker. Constr. Build. Mater. 280. https://doi.org/10.1016/j.conbuildmat.2021.122510.